1   **Moisture Pathways into the US Intermountain West Associated with Heavy Winter**

2   **Precipitation Events**

3

4   Michael A. Alexander[1], James D. Scott[1,2], Dustin Swales[1,2], Mimi Hughes[1,2], Kelly Mahoney[1,2],

5   Catherine A. Smith[1,2]

6

7   *1 NOAA/Earth System Research Laboratory, Boulder, Colorado*

8   *2 Cooperative Institute for Research in Environmental Sciences, University of Colorado*
9   *Boulder, Boulder, Colorado*
10
11
12
13
14
30   Corresponding Author address:
31
32   Michael Alexander
33   NOAA/Earth System Research Laboratory
34   R/PSD1, 325 Broadway
35   Boulder, CO 80305
36   E-mail: michael.alexander@noaa.gov

ABSTRACT

37

38   Two methods were used to identify the paths of moisture transport that reach the US

39   intermountain west (IMW) during heavy precipitation events in winter. In the first, the top 150

40   precipitation events at stations located within six regions in the IMW were identified, then back

41   trajectories were initiated at 6 hour intervals on those days at the four CFSR grid points nearest

42   the stations. The second method identified the leading patterns of integrated water vapor

43   transport (IVT) using the three leading Empirical Orthogonal Functions (EOFs) of IVT over land

44   that were first normalized by the local standard deviation. The top 1% of the associated 6-hourly

45   time series were used to construct composites of IVT, atmospheric circulation and precipitation.

46   The results from both methods indicate that moisture originating from the Pacific that leads

47   to extreme precipitation in the IMW during winter take distinct pathways through gaps in the

48   Cascade (Oregon-Washington), Sierra-Nevada (California) and Peninsula Mountains (southern

49   California through Baja California). The moisture transported along these routes appears to be

50   the primary source for heavy precipitation for the mountain ranges in the IMW. The synoptic

51   conditions associated with the dominant IVT patterns include a trough ridge couplet at 500 h PA,

52   with the trough located northwest of the ridge where the associated circulation funnels moisture

53   from the west-to-southwest through the mountain gaps and into the IMW.

54

55

1. Introduction

While generally dry, the interior of the western US can experience extreme precipitation events. For example, in early November 2006, a major rain and flood event occurred in portions of western Montana. One weather station in Glacier National Park recorded over 300 mm (12 inches) of precipitation between 3-8 November and the flow in the North Fork of the Flathead River reached 18,000 cubic feet per second on 8 November exceeding the previous November record by ~40% (Berhardt 2006; Neiman et al. 2008). Extreme precipitation events can also occur over the southwest US during winter, e.g. in late January 2010 a series of three strong storms caused record precipitation and widespread flooding in central Arizona. How does the moisture penetrate the high terrain and complex topography near the US west coast in sufficient amounts to produce extreme precipitation events in the intermountain west (IMW)? Since flow over mountain causes air to cool and thus hold less moisture, air parcels likely take unique pathways through mountain gaps and/or have multiple moisture sources in order to retain enough water vapor to produce intense winter precipitation events in states such as Arizona, Colorado, Idaho and Utah.

Long narrow bands of enhanced water vapor transport generally located ahead of cold fronts, termed atmospheric rivers (ARs, Newell et al. 1992; Zhu and Newell 1998), are associated with heavy rain and snow events along the US west coast (Neiman et al. 2002; Ralph et al. 2004; Ralph et al. 2006, Nieman et al. 2008, 2011; Ralph and Dettinger 2011). Observational studies of strong winter storms over California lead to the identification of key ingredients for heavy precipitation in the Coastal and Sierra Nevada Mountains, including: an ARs transporting warm moist air from the subtropical Pacific (known colloquial as the "Pineapple Express", McGuirk et al. 1987, 1988; Lackmann and Gyakum 1999), upslope flow

79   with the atmospheric moisture transport being normal to the topography, a landfalling low-level

80   jet, low static stability, and strong upper-level dynamics (Pandey et al. 1999; Neiman et al. 2002;

81   Ohara et al. 2009). Further inland, the structure and evolution of storms and their associated

82   precipitation are greatly altered by upstream mountain ranges, such as the Cascades and Sierra

83   Nevada. For example, the classical model of a extratropical cyclone with strong near surface

84   fronts often fails in the IMW, where many storms only have elevated baroclinic zones (Marwitz

85   1980; Schultz et al. 2002).

86   Recent studies indicate that ARs could move inland and contribute a significant fraction

87   (10%-50%) of wintertime precipitation in the IMW (Leung and Qian 2009; Dettinger et al. 2011;

88   Rutz and Steenburgh 2012). Some pathways for inland ARs have been identified. Rutz and

89   Steenburg (2012) found that ARs that traverse Baja California contribute significantly to

90   precipitation in Arizona, exemplified by the extreme precipitation/flooding event that occurred in

91   Arizona in January of 2010 (described above) that penetrated through gaps in the mountains

92   along the Baja Peninsula (Neiman et al. 2013 and Hughes et al. 2014). Using combined

93   Empirical Orthogonal Functions (EOFs) of zonal and meridional integrated water vapor

94   transport, Rivera et al. (2014) identified two AR patterns that cause heavy winter precipitation in

95   the Verde River basin in central Arizona, one originates near Hawaii and crosses central Baja

96   California mainly from the west before turning north, and the second originates in the eastern

97   tropical Pacific and crosses southern Baja California from the southwest. Rutz et al. (2014) found

98   that ARs could penetrate into portions of the northwest and into the southwest, including central

99   Arizona, but appeared to be blocked by the high Sierras in California. The Great Salt Lake can

100   also act as a regional source of moisture for heavy precipitation in northern Utah (Steenburg et al

101   2000, Steenburg 2003). While the aforementioned studies have identified some of the moisture

4

102 sources for the IMW, the moisture pathways leading to heavy precipitation in the IMW during

103 winter have not been examined systematically.

104 Air parcel trajectories have been used to identify the sources and transport of moisture,

105 including those associated with ARs. Knippertz and Wernlie (2010) developed a climatology of

106 tropical-to-extratropical trajectories of moist air that identified the Pineapple Express as one of

107 the four main pathways although the trajectories with strong moisture transport that reach the

108 coast of Western North America may also have midlatitude origins (Roberge et al. 2009, Neiman

109 et al. 2013). Using air parcel movements calculated backward in time, or back trajectories, Bao

110 et al. (2006) found that while some of the moisture within ARs that reached the west coast of the

111 United States originated in the tropics much of it resulted from evaporation and moisture

112 convergence in midlatitudes in the warm sector of extratropical cyclones. Back trajectories have

113 also proved useful in understanding precipitation processes and diagnosing moisture sources in

114 other mountainous areas including the Appalachian Mountains (Konrad 1994; Perry et al. 2007;

115 Furman and Konrad 2013).

116 Extreme precipitation events can cause severe flooding, potentially leading to safety and

117 infrastructure problems. Determining how these events occur in the IMW (taken here to be

118 between the Sierra Nevada/Cascade Mountains and the Continental Divide) would help water

119 managers and emergency planners better prepare for these extreme precipitation events. For

120 example, the Bureau of Reclamation operates hundreds of dams in the IMW and a detailed

121 understanding of the sources of moisture and processes leading to heavy precipitation would

122 inform decisions about dam safety and flood hydrology.

123 Here we investigate the following questions associated with extreme precipitation events in

124 the US IMW during winter:

125　　• Are there dominant moisture pathways?

126　　• Do they differ for different regions in the IMW?

127　　• Does much of the moisture transport occur through narrow gaps in the mountains, or can

128　　　moisture remain in the atmosphere after passing over higher topography?

129　　• What synoptic features are associated with the moisture transport?

130　　We will address these questions using two complementary methods: air-parcel trajectories

131　provide a Lagrangian approach for identifying regional pathways into the IMW, while Empirical

132　Orthogonal Function (EOF)/Principal Component (PC) analyses of integrated water vapor

133　transport provide a large-scale Eulerian view of the dominant moisture pathways and the

134　associated synoptic conditions. The precipitation data and atmospheric reanalysis used in this

135　study are described section 2 along with methods used to compute trajectories and EOFs/PCs.

136　The results are presented in section 3 and summarized and discussed in section 4.

137

138　2. Data and Methods

139　　We use a combination of data sets and methods to identify the moisture pathways and

140　synoptic conditions associated with heavy precipitation events in the IMW during 1979-2010,

141　the period when high-resolution atmospheric reanalysis is available.

142

143　*a) Station precipitation data*

144　　We obtained daily precipitation data from the Global Historical Climatology Network

145　(http://www.ncdc.noaa.gov/oa/climate/ghcn-daily/; Durre et al. 2008, 2010; Menne et al. 2012)

146　to identify heavy precipitation events. We only included stations that had more than 20 years of

147　data where less than 20% of the days were missing observations during 1979-2011 to ensure a

148   reasonable climatology at each station. The stations were grouped into six regions covering most

149   of the IMW including: 1) eastern Washington, northern Idaho and southeastern British Columbia

150   (hereafter WA-nID) ; 2) eastern Oregon and southern Idaho (OR-sID); 3) Nevada (NV); 4) Utah

151   and western Colorado (UT-CO); 5) southeastern California, western Arizona and southern

152   Nevada (sCA) ; and 6) Arizona and New Mexico (AZ-NM; Fig. 1). While the choice of regions

153   is subjective, their number and boundaries were based on a number of considerations, including:

154   *i)* that regions have more than 50 stations (and all but NV and sCA have more than 100); *ii)* the

155   location of topographic features, e.g. selecting mountain chains for some of the regional

156   boundaries; *iii)* grouping stations that exhibited similar absolute or relative precipitation maxima,

157   e.g. many of the stations in the sCA region exhibited daily precipitation maxima that had a

158   relatively small magnitude but made a substantial contribution to the annual precipitation; and *iv)*

159   the regions with integrated water vapor transport (IVT) maxima based on the EOF analysis (see

160   Section 3.b).

161   To focus on the heaviest events in our record, we first identified the 150 maximum one-day

162   precipitation amounts during 1979-2011 (~2.5% of winter days) at stations within each of the six

163   regions shown in Fig. 1. The precipitation events are independent in that only the station with the

164   maximum on that day is included. The maximum 150 one-day precipitation values within a

165   region are shown in Fig. 2a via color shading (stations included in the analysis but without a top

166   event are shown by open circles; some stations recorded more than one event). The precipitation

167   amounts over the IMW range from approximately 25-175 mm, with all regions except NV

168   having at least one station with more than 100 mm. The greatest one-day totals (> 125 mm) are

169   found in the central WA-nID, central OR-sID, northern sCA, and western AZ-NM regions.

170   The percentage of the top 150 events occurring at a particular station in each of the regions is

171   shown in Fig. 2b. Less than 5% of the events occur at most stations in all six regions in the

172   domain. However, the extreme events are not uniformly distributed across a given region: many

173   stations do not have a precipitation event in the top 150, but there are a few stations at which

174   10% or even 15% of the extremes occur. The concentration of extreme events at just a few

175   stations is most pronounced in the WA-nID, AZ-NM and sCA regions where only three stations

176   account for ~40% of the cases.

177

178   *b) CFSR*

179   The primary source for the gridded atmospheric fields used here is the Climate Forecast

180   System Reanalysis (CFSR, Saha et al. 2010) from the National Centers for Environmental

181   Prediction (NCEP). The CFSR is global and includes atmosphere, ocean, land and sea ice

182   models, and an assimilation system to merge the model first guess fields with observations. The

183   resolution of the spectral atmospheric model is T382 (~40 km) with 64 vertical levels, which is

184   nearly an order of magnitude finer than NCEP reanalysis (versions 1 and 2) used in many

185   previous AR studies (e.g.). The CFSR analysis fields are archived on a 0.5° latitude and

186   longitude grid at 6-hour intervals from January 1979 to March 2011.

187

188   *c) Livneh precipitation data*

189   We also use gridded precipitation values from a high-resolution (1/16°) data set recently

190   developed by Livneh et al. (2013) available over the conterminous United States and the

191   Columbia River Watershed in southwest Canada for the years 1915 – 2011. It is an updated

192   version of the Maurer et al. (2002) data set and derived using daily observations from

193   approximately 20,000 NOAA cooperative observer stations. The daily data are rescaled so that

194   the long-term monthly climatology equals that from the parameter-elevation regressions on

195   independent slopes model (PRISM; Daly et al. 1994). The Livneh dataset likely provides a better

196   representation of precipitation than CFSR in the IMW due to its higher resolution and explicit

197   treatment of topography.

198

199   *d) Trajectories*

200   Backward (in time) air parcel trajectories, based on the three-dimensional wind field obtained

201   from CFSR were computed using a method originally developed at the University of Melbourne

202   (http://www.cycstats.org/trajectories/trajhome.htm; Noone and Simmonds 1999; Barras and

203   Simmonds 2009), which we modified to provide additional output including the surface pressure.

204   Trajectories were computed for the top 150 one-day precipitation totals (as defined in section

205   2.a) that occurred at stations within each of the six regions shown in Figs. 1&2. The trajectories

206   were initiated from the four CFSR grid points surrounding the station that recorded extreme

207   precipitation event and were initiated at the four 6-hour intervals on the day the event occurred.

208   In the vertical, we examined trajectories initiated on pressure levels from 600 hPa down to the

209   surface at 50 hPa increments (e.g. 600, 650, 700, etc.). For the results presented here, we used

210   trajectories starting at a single pressure level located between 50 and 100 hPa above (at a lower

211   pressure than) the surface. For example, if the surface pressure was 827 hPa, trajectories were

212   initiated at 750 hPa level. We chose this level, which is generally located in the upper boundary

213   layer/lower free troposphere, because it was high enough so that nearly all (> 99%) of the

214   trajectories remained above the surface over North America but was low enough to be located

215   within the region of strong water vapor transport (e.g., see Neiman et al. 2013, Rivera et al.

216 2014). A total of 2400 trajectories (150 independent events **x** 4 CFSR grid points **x** 4 times per

217 day) were initiated in each region. The position of a trajectory is computed backwards in time

218 over the five previous days at one-hour intervals using the six-hourly three-dimensional CFSR

219 wind fields.

220   The results from the trajectory analysis will be influenced by several factors, including the

221 location of stations within a region and the frequency with which they get heavy precipitation.

222 The individual trajectories will also be influenced by the resolution of the CFSR, which is

223 relatively fine compared to most reanalyses, but is still coarse (~40 km) relative to the

224 topographic features in the western US. The trajectories are also not tracking moisture directly

225 but represent air parcels initially located near the station recording heavy precipitation; it is

226 possible that some trajectories track a drier sector of a given storm.

227

228 *e) EOFs of IVT*

229   We also examine moisture pathways and associated synoptic variability using EOFs of the

230 integrated water vapor transport (IVT). The IVT was derived from CFSR winds ($\vec{V}$) and specific

231 humidity (q) on mandatory pressure levels that were vertically integrated from the surface to 300

232 hPa ($\sum_{300\ hPA}^{Psfc} \vec{V} q\ \Delta p/g$) The IVT was computed at 6-hr intervals during winter (Oct-Mar) from

233 1979 to 2011. The mean and standard deviation of IVT over the domain (25°N-60°N, 150°W-

234 105°W) both exhibit a maximum at ~40°N, 145°W over the Pacific that extends northeastward

235 towards the northwest US (Fig. SM1). Given that IVT variability is greater over the Pacific and

236 along the US west coast than in the IMW, we took several steps to highlight IVT patterns in the

237 IMW prior to calculating the EOFs. First, IVT anomalies were computed by subtracting the

238 monthly means from the total field and were then normalized by dividing the anomaly values by

10

239 the standard deviation of the 6 hourly data over all years in a given calendar month. Finally, the

240 EOFs were computed using only land points. We examine the three leading EOFs and use their

241 associated PCs to identify when the patterns of IVT and other variables are of large amplitude.

242

243 **3   Results**

244 *a.   Trajectory analysis*

245   To illustrate air parcel paths, example backward trajectories were initiated on four different

246 days at the four CFSR grid points surrounding stations that recorded heavy precipitation in the

247 OR-sID region (Fig. 3). While all of the trajectories came from the Pacific, they indicate that

248 moist air parcels can still take diverse routes to reach the lower troposphere over southwest Idaho

249 including central and northern California, Nevada and Oregon (Fig. 3a), central Oregon (Fig.

250 3b&d), and southern California and Nevada (Fig. 3c). Some of the trajectories indicate slower

251 and/or more circuitous routes, e.g. two loop over northern California, while several others

252 meander over the Snake River Plain in southwest Idaho for trajectories reaching southeast Idaho

253 on 20 Nov 2010 (Fig. 3d). All trajectory segments occur at pressures (color shading) greater than

254 700 hPa. The trajectories that pass through central Oregon remain at relatively low pressures

255 (approximately 700-800 hPa; relatively high elevations) over the Cascade Mountains, while

256 those that pass through northeastern California are located at higher pressures over California's

257 central valley and remain at relatively high pressure (> 800 hPa) while passing north of the high

258 Sierra Nevada. The trajectories for 11 Mar 1995 illustrate a different path: the trajectories come

259 from the south and stay at relatively low pressure over land; they parallel the high narrow

260 mountain ranges in Nevada and pass through a relatively low point in the mountains in southern

261 California, near ~35°N, 117°W.

262   To determine if the air parcels leading to heavy precipitation have preferred routes, the

263   number of hour-long trajectory segments that end within a CFSR grid volume are counted. The

264   counts are performed for the back trajectories for the top 150 events (16 trajectories per event)

265   initiated in each of the six regions and presented as maps of the number of trajectory points

266   throughout a given CFSR column, and as cross sections of the number of counts as a function of

267   height along a transect (indicated by the black line in Fig. 1) spanning the highest portions of the

268   Cascade, Sierra and the Peninsula Mountains (north-south range extending from east of San

269   Diego through Baja California).

270   Count maps and cross sections for the three northern regions (i.e., WA-nID; OR-sID and

271   NV) are presented in Fig. 4. Broad scale aspects of the topography are also shown on the maps.

272   The count map for the WA-nID region (Fig. 4a) shows the greatest number of trajectory

273   segments in northern Idaho and over southeast Washington, which corresponds with the area

274   where backward trajectories are initiated (Fig. 2). Further west, the axis of higher count values

275   continues along the Washington/Oregon border, over northwest Oregon and the Pacific. While

276   the count map indicates that trajectories can occur across much of the northwest US from central

277   California to the Canadian border (counts > 50), the majority of the trajectories appear to move

278   through the Columbia River Gorge Gap in the Cascade Mountains (as indicated by the break in

279   the 1000 m contours at ~45.5°N, 122°W) and continue along the Columbia River valley. Flow

280   through this gorge is supported by the cross section of the number of trajectories originating in

281   WA-nID, in that the greatest number of trajectories pass through the mountains below 800 hPa at

282   45°N in the v-shaped notch in the topography (Fig. 4b). A modest secondary maxima occurs

283   over central California and passes through an elevated gap in the mountains at ~41°N, to the

284   north of the high Sierras.

285   The count map and cross section for the OR-sID region, shown in Figs. 4c&d, show a very

286   different pathway than the trajectories that impact northern Idaho. Along the coast the

287   trajectories extend from the Oregon-Washington border to central California but with a preferred

288   path over the Sacramento Valley (northern portion of the central valley), across northeastern

289   California and northwestern Nevada and into southern Washington and Idaho. The map and

290   cross section for this region indicates that the trajectories pass to the north of the high Sierra's

291   through a gap (near Burney, CA) at ~41°N and over a lower elevation portion of northwest

292   Nevada. Upon reaching Idaho many trajectories follow the Snake River Plain, which has a bow-

293   shape and extends across all of southern Idaho. The counts also suggest a secondary path over

294   the Cascades and across Oregon.

295   The count map and cross section for the NV region (Fig. 4 e&f) indicate that the highest

296   portion of the Sierras, which extend along a northwest-southeast axis between about 35° and 38°

297   N, are a barrier which most air parcels flow around. One trajectory path is just to the north of the

298   high Sierra, with higher counts over north central Nevada, while a second extends over southern

299   California and into southern Nevada. Downstream of the Sierra Nevada, there are a higher

300   number of counts between the two branches suggesting that the moisture flow may fill in on the

301   leeward side of the mountains. The relatively high elevation (and low pressure) that the air

302   parcels take to reach NV, especially for the northern route, may limit the amount of moisture

303   they carry and contribute to the lack of extreme precipitation in this region.

304   Maps and cross sections for the three southern regions, UT-CO, sCA and AZ-NM are shown

305   in Fig 5. For all three, the majority of the routes pass over the Pacific and into California or Baja

306   California. The primary axis for the maximum trajectory counts for the UT-CO region (Fig. 5a),

307   is similar to the southern branch for the NV region, i.e. across southern California and Nevada

308 but now extends into western Utah along the western side of the Wasatch Mountains. A

309 secondary area of high trajectory counts extends along the Utah/Arizona border, where the

310 terrain is relatively low, and continues into southwest Colorado, where there is another

311 maximum near the San Juan Mountains. Some air parcels reaching UT-CO during heavy

312 precipitation events enter the US from the south including the Gulf of California. The

313 accompanying cross-section (Fig. 5b) indicates that the highest number of trajectories pass south

314 of the high Sierras at ~35°N between 900 and 750 hPa near a gap in the mountains.

315 The majority of the back trajectories in sCA were initiated and traverse the southern portion

316 of the region (Fig. 5c), which they reach by either utilizing a zonal path near the border with

317 Mexico or by crossing northern Baja California near ~29°N and then going north over the Gulf

318 of California. The accompanying cross-section (Fig. 5d) indicates that both paths utilize

319 mountain gaps where more trajectories pass through the northern gap.

320 The trajectory count maximum occurs in the western part of AZ-NM region (Fig. 5e) in the

321 vicinity of the Mogollon Rim, where many extreme precipitation events occurred. The pathways

322 for the AZ-NM are similar to those for the sCA region, except that more trajectories utilize the

323 southern gap at ~29°N (Fig. 5f), which is wider and deeper than the one near the border.

324 Count maps of back trajectories over six-hour intervals (e.g. 0-6, 6-12 hours, etc.) are shown

325 for all six regions in the supplementary material. Going forward in time, air parcels extending

326 over a wide swath of the North Pacific propagate to the west/northwest and generally cross the

327 west coast of North America 24-36 hours prior to reaching the target region (Figs. SM2-7).

328 How unique are these pathways; i.e. are the trajectories on all winter days in general similar

329 to or different than those associated with extreme precipitation events? To address this question

330 we randomly selected days and locations (which could include those with extreme events) to

331 initialize the back trajectories as follows: for each region we determine the stations at which the

332 top 150 events occurred, then randomly select one of these stations and a date between October

333 and March from 1979-2011 using a random number generator. As in the extreme cases,

334 trajectories were initiated at the four CFSR gridpoints nearest to the station and at four six-hour

335 intervals on the randomly chosen day. This procedure was repeated 300 times based on the

336 number of trajectories needed to obtain stable count results for the random cases; the counts were

337 then scaled by dividing by two so they could be directly compared with the 150 extreme cases.

338 Count maps and cross sections for the randomly generated trajectories in the northern and

339 southern regions are shown in Figs. SM8&9, while the difference in the counts between the

340 extreme and randomly generated trajectories are shown in Figs. 6&7.

341 The general patterns of the count maps and cross sections for the random generated

342 trajectories (Figs. SM8&9) are similar to those based on the extreme cases in all six regions

343 (Figs. 4&5). For example, as in the extreme cases, a large fraction of the trajectories at randomly

344 selected stations/days for the WA-nID region follow the Columbia River valley passing through

345 the gap in the Cascades. However, consistent differences between the two are apparent as well.

346 The back trajectory counts within the boundaries of all six regions are lower in the extreme

347 compared to the random cases (Figs. 6&7). This suggests faster movement of the air parcels, i.e.

348 fewer trajectories remain in the target region over time, and likely more moisture transport by

349 stronger winds during winter periods with extreme precipitation. In addition, the back trajectories

350 exhibit a more southwesterly path and are generally lower in the atmosphere in the extreme

351 compared to the random cases. For example, in the OR-sID region (Fig. 6c&d), the number of

352 trajectories passing through California and the gap north of the Sierras increases and the number

353 of trajectories through the Columbia Gorge gap decreases in the extreme relative to the random

354   cases; there are also fewer trajectories on extreme days above (at pressures less than) 700 hPA.

355   One anticipates that air parcels originating further north and/or at higher elevation would be

356   cooler and carry less water vapor. This analysis suggests, that while the pathways into the

357   interior west on days with heavy precipitation might not be unique, strong flow from the

358   southwest at lower elevations is effective at funneling moisture through the mountain gaps.

359

360   *b) EOFs and PC based composites*

361   The three leading EOFs of IVT are shown in Fig. 8a; recall that the EOFs are computed using

362   normalized IVT values over land, so they are better able to depict the patterns of variability in

363   the IMW. The dominant pattern, which explains 28.5% of the variance, has one sign over the

364   western US with a maximum in southern Oregon/Idaho. The 2nd EOF, which explains 23.8% of

365   the variance, exhibits a meridional dipole of IVT, with centers over Arizona and along the US-

366   Canada border and the third EOF, which explains 9.9% of the variance, has anomalies of one

367   sign over California and Nevada and anomalies of the opposite sign over the rest of the land

368   points in the domain. The three leading EOFs exhibit broad spatial patterns and explain more

369   than 60% of the variability over the western US.

370   Histograms of the three leading PCs are shown in Fig. 8b, where the PC indicates the

371   amplitude and phase of the associated EOF pattern over time. The histogram of PC 1, is highly

372   skewed towards positive values, indicating large positive IVT anomalies into the western US,

373   where EOF 1 exhibits maximum variance, are much more common than large negative

374   anomalies. This is consistent with the atmospheric river concept, with a strong narrow band of

375   water vapor transport during storms, and weak/diffuse dry conditions between storms. The

376   second and third PC also exhibit positive skew but not to the extent of PC 1.

377   EOFs maximize the explained variance over the entire domain and the patterns are required

378   to be orthogonal in both space and time, which can result in nonphysical patterns. This is

379   especially the case for lower order EOFs/PCs. Here the first two leading EOFs, which explain a

380   large fraction of the variance, are separable from the remaining EOFs, while EOF 3 may not be,

381   as the fourth EOF explains 7% of the variance. We examine the synoptic conditions associated

382   with the leading EOFs using PC-based composites of the full anomaly fields but modify the

383   compositing method (described below) to extract realistic synoptic patterns associated with

384   EOF/PC 3.

385   The EOF analysis was performed using IVT anomalies during all cold season days at 6 hr

386   intervals; since we wish to focus on extreme events, composites were constructed based on when

387   the largest amplitude values (> |99%|) of the three leading PCs occurred. We used the upper 1%,

388   an average of 232 cases, as opposed to the top 150 cases (~2.5%) as done for the precipitation-

389   based trajectory analysis, as here we are using 6 hourly rather than daily values. (The PC-based

390   composites using the top 2.5% of the values <not shown> are similar to the ones presented below

391   albeit with weaker amplitude.) Since EOF 1 covers the entire western US and heavy precipitation

392   is likely associated with large positive IVT PC 1 values, "high" composites are constructed only

393   for periods with large positive PC values. For EOF/PC 2, positive values are associated with

394   strong IVT into the southwest US, while large negative values indicate strong transport over the

395   northern tier states; thus both high and "low" (bottom 1%) composites are constructed for this

396   PC. The pattern identified by EOF 3 suggests the potential for strong IVT anomalies both near

397   the southern and northern border for positive PC 3 values, while negative PC 3 values are

398   associated with positive IVT anomalies in central California. Since the latter would mainly lead

399   to precipitation in the high Sierras but not in the IMW, we will construct composites using

400   positive PC 3 values.

401   The synoptic conditions associated with high PC 1 values are illustrated via composite maps

402   (including values over the ocean) of the non-normalized anomalous IVT magnitude, direction,

403   and convergence (-∇·IVT), the specific humidity (q) at 700 hPa, 500 hPa height, and

404   precipitation from CFSR and the Livneh data set. The composite IVT maps (Fig. 9a&b) show

405   large IVT anomalies extending northwestward from the subtropical Pacific into the northwest US

406   consistent with a strong AR coming onshore in Oregon and California. Smaller-scale IVT

407   anomalies suggest two pathways towards the interior: one through northern Oregon and into

408   Washington, northern Idaho and Montana and a second over central California then extending

409   northeastward across northern Nevada, southern Idaho and extending into Wyoming. The water

410   vapor anomalies (Fig. 9c) emphasize the southern of these two routes and resembles the main

411   trajectory pathway associated with heavy precipitation events in the OR-sID region (*cf.* Fig. 4c).

412   The anomalous circulation exhibits a trough centered west of Vancouver Island and a ridge over

413   the southwest (Fig. 9d). Both the ridge and trough exhibit a southwest to northeast tilt, with a

414   strong gradient between them especially over the northwest US. Assuming geostrophic flow, the

415   height anomalies are consistent with the cyclonic (counterclockwise) IVT vectors west of

416   Canada and anticyclonic (clockwise) IVT west of Baja California with strong onshore flow of

417   moisture into the western US. The anticyclonic IVT center is located west of the 500 hPa ridge

418   due to larger mean values of q over the Pacific Ocean than the western US, so the winds

419   transport much more water vapor onshore. Lead/lag sea level pressure (SLP) anomaly

420   composites (Fig. SM10) indicate that a low pressure anomaly over the northeast Pacific

421   intensifies and moves northeastward over the two days before reaching a maximum near

18

422 Vancouver Island (at zero lag, concurrent with the other composite fields). The SLP anomaly

423 exhibits a more zonal structure and extends further inland than the trough at 500 hPa.

424 The IVT exhibits strong convergence (Fig. 9b, green shading) over the Sierra and Cascades

425 from California to southern Canada and along the coastal range in northern California. A

426 secondary maximum is clearly evident over mountainous regions of Idaho and western Montana.

427 These results indicate that the moisture transport identified by IVT EOF 1 doesn't just pass

428 through the IMW but converges over the western mountain ranges, with corresponding weak

429 anomalous moisture divergence on the leeward side of some mountains. While a detailed

430 moisture budget analysis is beyond the scope of this study, the convergence of IVT ($-\nabla \cdot$IVT) is

431 primarily balanced by precipitation minus evaporation plus the time tendency of the column-

432 integrated moisture (e.g., Newman et al 2012 and references therein). Since evaporation and the

433 moisture tendency are generally smaller than the other budget terms during winter over the IMW

434 (e.g. Smith and Kummerrow 2013), the IVT convergence and precipitation patterns should be

435 similar. Indeed, the composite maps of precipitation (Fig. 9e&f, note smaller domain relative to

436 other maps) are very similar to those of $-\nabla \cdot$IVT (Fig. 9b). This is consistent with the orographic

437 driver of winter precipitation in the IMW, with moisture transported from the Pacific Ocean into

438 the interior precipitating out when the air impinges on mountain ranges. While the broad pattern

439 of the precipitation anomalies in CFSR and Livneh data sets (Figs. 9e & f, respectively) are

440 similar, fine scale features are much better resolved in the high-resolution Livneh data set and are

441 clearly influenced by the local topography. For example, anomalous heavy precipitation

442 associated with PC 1 occurs near the peaks in the Sawtooth and Salmon River Mountains in

443 central Idaho but the anomalies are negligible just to the south over the Snake River Plain (Fig.

444 9f).

445   The PC2 high composite exhibits enhanced moisture transport from the Pacific Ocean, across

446   southern California and the Baja Peninsula, and into the southwestern US (Fig. 10a&b). Within

447   this broad region, there are two enhanced regions of IVT and 700 hPa q, one along the

448   US/Mexico border and the other across Baja California at approximately 29-30°N (Fig. 10a&c),

449   where the topography is generally less than 800 m, relatively low areas in the Peninsula

450   Mountains. These enhanced areas of IVT transport are consistent with the major paths for

451   trajectories that traverse southern California and Baja California for heavy precipitation events in

452   the three southern regions, especially sCA and AZ-NM (Fig. 4). The circulation anomalies

453   exhibit a wave train with a large trough centered over Oregon/Northern California flanked by

454   ridges to the northwest and southeast, with a strong gradient in the height field from southern

455   California/northern Baja California northeastwards towards Wyoming. The associated SLP

456   anomaly propagates eastward and becomes zonally elongated and centered further east than the

457   500 mb anomaly (at zero lag) along the border between Idaho, Nevada and Utah (Fig. SM11).

458   The anomalous moisture flux convergence resulting from this flow is extensive (Fig. 10b), with

459   large -∇·IVT values and heavy precipitation in the Sierra and Peninsula Mountains in California

460   but also in the interior including the Mogollon Rim in Arizona, the Wasatch Mountains in Utah

461   and the San Juan Mountains in southwest Colorado (Fig. 10e&f).

462   The PC 2 low composite features IVT anomalies with a long fetch across the eastern Pacific

463   extending from ~25°N, 145°W to the Pacific Northwest where it turns and extends eastward

464   along the Canadian border (Fig. 11a&b). A local maximum in IVT and q extend across

465   Washington, northern Idaho and into Montana (Fig. 11a,b&c), which is consistent with the

466   trajectory path leading to heavy precipitation in the WA-nID region (Fig. 4a). The 500 hPa

467   height pattern features a ridge centered over the IMW and a trough off the Canadian coast, which

468 are elongated along a southwest-northeast axis (Fig. 9d). As in the previous composites, the

469 anomalous SLP is zonally elongated with a strong gradient along its southern flank, here parallel

470 to the US/Canadian border (Fig. SM12). Strong IVT convergence and heavy precipitation occurs

471 over the Olympic and Cascade Mountains in western Washington and southern British Columbia

472 with a secondary maxima over northern Idaho and southeast British Columbia (Fig 11b,e,f).

473 However, there is anomalous IVT divergence but positive precipitation anomalies in a few

474 narrow meridional bands, such as in central Washington and western Montana extending

475 northwest into Canada. These occur in the lee of mountains and are likely associated with

476 subsidence and drying. This apparent discrepancy with enhanced precipitation in these regions

477 may be due to several factors including: i) enhanced evaporation compensating for the moisture

478 divergence; ii) a non-negligible decrease over time in the column-integrated moisture content;

479 and iii) after assimilation of observations the moisture budget is not balanced in CFSR (or other

480 reanalyses). Weak negative precipitation anomalies also occur over northern California and

481 Colorado.

482 To determine if EOF 3 represents a coherent pattern we first regressed out the contribution of

483 both EOF 1 and 2 from the full anomaly fields at each time step (the original EOF 3 becomes the

484 leading pattern of the remaining variance). We then computed the correlation between regional

485 averages of the IVT anomalies in the northern center of this EOF (northern Washington; 48°-

486 50°N, 120°-118°W) and the southern center (northwestern Mexico; 28°-30°N, 111°-109°W),

487 which have the same sign (Fig. 8). The correlation between the two regions is -0.07 for all days

488 and -0.25 for the top 1% of the PC values. This suggests that the IVT in the two regions,

489 associated with the original EOF/PC3 are not strongly related but are an artifact of the analysis

490 technique. (In the full data set the two regions are strongly anti-correlated (r=-0.83), due to the

491   out-of-phase relationship between IVT anomalies in these two areas associated with EOF/PC 2).

492   The atmospheric circulation associated with the positive phase of EOF 3 includes a relative

493   small-scale "cut-off" low-pressure center located just west of northern Baja California (not

494   shown). Cutoff lows are fairly common in the wintertime circulation and can cause heavy

495   precipitation in the southwest US (Knippertz and Martin 2007) and are different from the

496   weather patterns associated with the first two EOFs.

497   The following procedure is used to construct composites that isolate the cutoff lows and the

498   related IVT and circulation anomalies over the southwest. First, based on the full anomaly fields,

499   we identify 6-hr periods with the top 1% of PC 3 values. Next we exclude periods that are in the

500   top or bottom 1% of PC 2 cases, as PC 2 strongly influences IVT in the southwest US. Finally,

501   we retain events where the IVT anomaly is positive in the southern center of EOF 3 located over

502   northwest Mexico. We retain 116 cases that pass these criteria to construct a composite. The

503   composite indicates enhanced IVT transport and q over southern Baja California, the Gulf of

504   California, northwest Mexico and into southern Arizona and New Mexico (Fig. 12). While the

505   topography in northern Mexico is relatively high, moisture may be able to move through the

506   north-south oriented mountain valleys of northern Mexico and over the low topography along the

507   eastern shore of the Gulf of California. Moisture can also propagate inland from the Gulf of

508   California into Arizona along the Colorado and Gila River valleys. The 500 hPa (Fig. 12d) and

509   SLP field (Fig. SM13) exhibit a cutoff low, just west of northern Baja California with a weak

510   trough to the north, from which the cutoff may have been linked to at a previous time. Over the

511   US, the precipitation exhibits a maximum over the Mogollon Rim in Arizona and western New

512   Mexico. These circulation and precipitation anomalies closely resemble the "Type 2" AR events

513   identified by Rivera et al. (2014). Enhanced precipitation also occurs over western Washington,

514   likely associate with the weak trough located to the north, perhaps indicating a link between

515   precipitation in the northwest and southwest US identified in the original EOF 3.

516

517   **4.   Summary and Discussion**

518   Two complementary methods were used to identify the paths that moisture takes to reach the

519   US intermountain west that contribute to heavy precipitation events during winter. In the first,

520   the top 150 precipitation events at stations located within each of six regions in the IMW were

521   identified, then back trajectories were initiated on those days at the four CFSR grid points nearest

522   the stations. While the trajectories track air parcels and not moisture explicitly, by initiating the

523   parcels relatively close to the surface (within 50-100 hPa of the SLP) where the moisture is

524   concentrated, the trajectories should provide a reasonable representation of water vapor

525   movement. The second method identified the leading patterns of integrated water vapor

526   transport, using the three leading EOFs of IVT over land that were first normalized by the local

527   standard deviation. The top 1% of the associated PCs were used to identify 6 hr periods in which

528   the amplitude of the EOF patterns were large and then composites of IVT, atmospheric

529   circulation and precipitation were computed using those periods. To focus on regions where

530   moisture transport was strong, composites were constructed using positive ("high") values of

531   PCs 1, 2 and 3 and negative ("low") values of PC2 (with large IVT along the Canadian border);

532   only a subset of these days were used in the PC3-based composites to better isolate realistic

533   synoptic conditions in the southwest US.

534   The results from both methods clearly indicate that moisture originating from the Pacific that

535   produces extreme precipitation in the IMW US during winter take dominant pathways through

536   gaps in the Cascade (Oregon-Washington), Sierra-Nevada (California) and Peninsula Mountains

537   (southern California through Baja California). The following paths for different regions were

538   identified (shown schematically in Fig. 13): 1) the Columbia River basin is a conduit for

539   moisture to reach eastern Washington, northern Idaho and western Montana; 2) a surprising path

540   from central and northern California, through a gap to the north of the high Sierras (~41°N), then

541   north into eastern Oregon and Idaho, into the mountains of central Idaho and along the Snake

542   River Plain; 3) through gaps to the north and south (~35ºN) of the high Sierras to reach Nevada;

543   4) through the gap just south of the Sierras into portions of Utah, Colorado and Arizona; and 5)

544   flow through gaps in the Peninsula Mountains near the US-Mexico border, at ~29ºN and over the

545   southern portion of the peninsula that has relatively low topography, bringing moisture to

546   Arizona and western New Mexico. These pathways are consistent with recent studies of the

547   penetration of atmospheric rivers into the IMW; i.e. Rutz and Steenburg (2012) found that the

548   high Sierras strongly block the inland penetration of ARs, while Neiman et al. (2013), Hughes et

549   al. (2014), Rivera et al. (2014), and Rutz et al. (2014), have found that water vapor transport

550   leading to heavy precipitation in the Mogollon Rim passes through low points in the mountains

551   of Baja California. The moisture transported along these routes appears to be the primary source

552   for heavy precipitation for the mountain ranges in the IMW including the Bitterroot Mountains in

553   northern Idaho, Salmon and Sawtooth Mountains in south/central Idaho, the Wasatch Mountains

554   in Utah, the San Juan Mountains in southwest Colorado and the Mogollon Rim in Arizona.

555   Several factors may influence the moisture pathways identified here. There can be two (or

556   more) pathways to a given region: e.g., air parcels that reach the WA-nID region from California

557   via the mountain gap to the north of the Sierras, in addition to the main pathway along the

558   Columbia River valley. A single pathway can also transverse more than one region; e.g. water

559   vapor transport through the gap south of Sierras can result in heavy precipitation in southeastern

24

560 California (sCA), eastern Nevada (NV), the Mogollon Rim (UT-NM), and the Wasatch and San

561 Juan Mountains in southwest Colorado (UT-CO). Also the station locations, which are usually

562 located in valleys likely miss extreme precipitation events at higher elevations and thus the

563 associated pathways. For example, the trajectory analysis did not clearly identify the path that

564 leads to heavy precipitation in the mountains of northern Colorado, such as the Gore or Park

565 Ranges (near ~40°N, 106.5°W). Thus, a more quantitative method for identifying regions (e.g.,

566 Bernard et al. 2013), including precipitation estimates from higher elevations and using finer

567 resolution data sets that better resolve gaps through the complex topography may lead to a more

568 precise depiction of the moisture pathways in the IMW. In addition, the influence of the seasonal

569 cycle, as well as lower frequency climate phenomena, such as ENSO, on ARs and the moisture

570 pathways into the IMW, warrant further study.

571   While the topography clearly influences the moisture transport and precipitation in the IMW,

572 it is the large-scale atmospheric circulation and synoptic conditions that ultimately shape the

573 conditions necessary for heavy precipitation to occur. For example, under some conditions the

574 flux of warm moist air may be strong enough so that not all of the moisture precipitates over the

575 Cascade Mountains and can thereby reach eastern Oregon and Idaho (see Figs. 4 and 7). In

576 addition, the pathways identified here are not limited to moist air (Figs. SM8&9). Air also flows

577 through these gaps from the west during dry conditions, albeit more from the north and at higher

578 elevations; e.g. trajectories reaching the OR-sID region often pass through the Columbia river

579 gap.

580   The general synoptic conditions associated with heavy precipitation events in the IMW

581 include a trough ridge couplet at 500 h Pa, with the trough located northwest of the ridge and a

582 tight gradient between them over and upstream of where the heavy precipitation occurs. The

583   accompanying circulation results in strong moisture transport from the southwest that reach a

584   maximum near the topographic gaps. While our analyses are based on precipitation and IVT over

585   the western US, the general circulation features are consistent with studies of ARs that impact

586   the Pacific coast and feature concentrated moisture transport ahead of a cold front that extends

587   thousands of kilometers southwestward over the Pacific Ocean. In addition to the large-scale

588   ridge and trough system in midlatitudes, smaller-scale cutoff lows, which move on shore at

589   ~30°N, can also transport tropical moisture across southern Baja and the Gulf of California

590   resulting in heavy precipitation over central Arizona (also see Knippertz and Martin 2007;

591   Rivera et al. 2014).

592   Determining potential pathways and sources for extreme precipitation events may help

593   inform decisions about dam safety, flood hydrology, and future monitoring. The trajectory and

594   EOF/composite analyses performed here could also provide useful indicators for short-term (1-2

595   day) predictions at dam sites and indicate the attributes of winter storms that generate the

596   heaviest precipitation in a given region.

597

604

605   **References**

Bao, J-W., S. A. Michelson, P. J. Neiman, F. M. Ralph, and J. M. Wilczak, 2006: Interpretation of enhanced integrated water vapor bands associated with extratropical cyclones: Their formation and connection to tropical water vapor. *Mon. Wea. Rev.*, **134,** 1063–1080.

606

607   Barras, V., and I. Simmonds, 2009: Observation and modeling of stable water isotopes as
608   diagnostics of rainfall dynamics over southeastern Australia *Journal of Geophysical*
609   *Research*, **114**, D23308, doi:10.1029/2009JD012132, 2009.

610

611   Bernhardt, D., 2006: Glacier National Park flooding November 2006. NWS Western Region
612   Tech. Attachment 08-23, 15 pp.

613

614   Bernard, E., P. Naveau, M. Vrac, and O. Mestre, 2013: Clustering of Maxima: Spatial
615   Dependencies among Heavy Rainfall in France. *J. Climate*, **26**, 7929–7937.

616

617   Daly, C., R. P. Neilson, and D. L. Phillips, 1994: A statistical-topographic model for mapping
618   climatological precipitation over mountainous terrain. *J. Appl. Meteor.*, **33**, 140–158.

619

620   Dettinger M. D., F. M. Ralph, T. Das, P. J. Neiman, and D. Cayan, 2011: Atmospheric rivers,
621   floods, and the water resources of California. *Water,* **3,** 445–478. DOI: 10.3390/w3020445.

622

623   Durre, I., M. J. Menne, B. E. Gleason, T. G. Houston, and R. S. Vose, 2010: Comprehensive
624   automated quality assurance of daily surface observations. *J. Appl. Meteor. Climatol.*, **49**,
625   1615-1633.

626

627   Durre, I., M. J. Menne, and R. S. Vose, 2008: Strategies for evaluating quality-control

628   procedures. *J. Appl. Meteor. Climatol*, **47**, 1785-1791.

629

630   Fuhrmann, C. M., C. E. Konrad, 2013: A Trajectory Approach to Analyzing the Ingredients

631   Associated with Heavy Winter Storms in Central North Carolina. *Wea. Forecasting*, **28**, 647–

632   667.doi: http://dx.doi.org/10.1175/WAF-D-12-00079.1

633

634   Hughes, M., K. M. Mahoney, P. J. Neiman, B. J. Moore, M. Alexander, and F. M. Ralph: The

635   landfall and inland penetration of a flood-producing atmospheric river in Arizona. Part II:

636   Sensitivity of modeled precipitation to terrain height and atmospheric river orientation. *J.*

637   *Hydromet.*, in press.

638

639   Knippertz, P., and J. E. Martin, 2007: A Pacific Moisture Conveyor Belt and Its Relationship to a

640   Significant Precipitation Event in the Semiarid Southwestern United States. *Wea.*

641   *Forecasting*, **22**, 125–144.

642

643   Knippertz, P., and H. Wernli, 2010: A Lagrangian Climatology of Tropical Moisture Exports to

644   the Northern Hemispheric Extratropics. *J. Climate*, **23**, 987–1003.

645   doi: http://dx.doi.org/10.1175/2009JCLI3333.1

646

647   Konrad, C. E., 1994: Moisture trajectories associated with heavy rainfall in the Appalachian

648   region of the United States. *Physical Geography*, **15**, 227-248. DOI:

649   10.1080/02723646.1994.10642514.

650

651   Lackmann, G. M., J. R. Gyakum, 1999: Heavy Cold-Season Precipitation in the Northwestern

652   United States: Synoptic Climatology and an Analysis of the Flood of 17–18 January 1986.

653   *Wea. Forecasting*, **14**, 687–700.

654

655   Lavers, D. A., G. Villarini, R. P. Allan, E. F. Wood, and A. J. Wade, 2012: The detection of

656   atmospheric rivers in atmospheric reanalyses and their links to British winter floods and the

657   large-scale climatic circulation. *J. Geophys. Res.*, **117**, D20106, doi:10.1029/2012JD018027.

658

659   Leung, L. R., and Y. Qian, 2009: Atmospheric rivers induced heavy precipitation and flooding in

660   the western US simulated by the WRF regional climate model. *Geophys. Res. Let.*, **36,**

661   DOI: 10.1029/2008GL036445.

662

663   Livneh, B., E. A. Rosenberg, C. Lin, B. Nijssen, V. Mishra, K. M. Andreadis, E. P. Maurer, D. P.

664   Lettenmaier, 2013: A Long-Term Hydrologically Based Dataset of Land Surface Fluxes and

665   States for the Conterminous United States: Update and Extensions. *J. Climate*, **26**, 9384–

666   9392.

667

668   Marwitz, J. D., 1980: Winter storms over the San Juan Mountains. Part I: Dynamical processes.

669   *J. Appl. Meteor.*, **19,** 913–926.

670

Maurer, E. P., A. W. Wood, J. C. Adam, D. P. Lettenmaier, and B. Nijssen, 2002: A long-term

hydrologically based dataset of land surface fluxes and states for the conterminous United

States. *J. Climate*, **15**, 3237–3251.

674

McGuirk, J. P., A. H. Thompson, and N. R. Smith, 1987: Moisture bursts over the tropical

Pacific Ocean. *Mon. Wea. Rev.*, **115**, 787–798.

McGuirk, J. P., A. H. Thompson, and J. R. Schaefer, 1988: An eastern Pacific tropical

plume. *Mon. Wea. Rev.*, **116,** 2505–2521.

675

Menne, M. J., I. Durre, R. S. Vose, B. E. Gleason, T. G. Houston, 2012: An Overview of the

Global Historical Climatology Network-Daily Database. *J. Atmos. Oceanic Technol.*, **29**,

897–910.doi: http://dx.doi.org/10.1175/JTECH-D-11-00103.1

679

Neiman, P. J., F. M. Ralph, A. B. White, D. E. Kingsmill, P. O. G. Persson, 2002: The Statistical

Relationship between Upslope Flow and Rainfall in California's Coastal Mountains:

Observations during CALJET. *Mon. Wea. Rev.*, **130**, 1468–1492.

doi: http://dx.doi.org/10.1175/1520-0493(2002)130<1468:TSRBUF>2.0.CO;2

684

Neiman, P. J., F. M. Ralph, G. A. Wick, J. D. Lundquist, and M. D. Dettinger, 2008:

Meteorological characteristics and overland precipitation impacts of atmospheric rivers

687   affecting the West Coast of North America based on eight years of SSM/I satellite

688   observations. *J. Hydrometeorology*, **9,** 22-47.

689

690   Neiman, P. J., L. J. Schick, F. M. Ralph, M. Hughes, and G. A. Wick, 2011: Flooding in Western

691   Washington: The Connection to Atmospheric Rivers. *J. Hydrometeorology*, **12,** 1337-1358.

692

693   Neiman, P. J., F. M. Ralph, B. J. Moore, M. Hughes; K. M. Mahoney; J. M. Cordeira and M. D.

694   Dettinger, 2013: The Landfall and Inland Penetration of a Flood-Producing Atmospheric

695   River in Arizona. Part 1: Observed Synoptic-Scale, Orographic, and Hydrometeorological

696   Characteristics. *J. Hydrometeorlogy*, **14**, 460-484.

697

698   Newell, R.E., Newell N. E., and C. Scott, 1992: Tropospheric Rivers? A pilot study. *Geophys.*

699   *Res. Lett.* **19**, 2401-2404. Doi:10.1029/92GL02916.

700

701   Newman, M., G. N. Kiladis, K. M. Weickmann, F. M. Ralph, and P. D.

702   Sardeshmukh 2012: Relative contributions of synoptic and low-frequency eddies to time-

703   mean atmospheric moisture transport, including the role of atmospheric rivers. *J.*

704   *Climate*, **25**, 7341-7361. doi: http://dx.doi.org/10.1175/JCLI-D-11-00665.1

705

706   Noone, D., and I. Simmonds, 1999: A three-dimensional spherical trajectory algorithm. Research

707   Activities in Atmospheric and Oceanic Modelling. Report No. 28, WMO/TD-No. 942. H.

708   Ritchie, Ed., World Meteorological Organization, 3.26-3.27.

709

710   O'Hara, M. L. Kaplan, S. J. Underwood, 2009: Synoptic Climatological Analyses of Extreme

711   Snowfalls in the Sierra Nevada. *Weather and Forecasting*, **24**, 1610-1624.

712

713   Pandey, G. R., D. R. Cayan, and K. P. Georgakakos, 1999: Precipitation structure in the Sierra

714   Nevada of California during winter. *J. Geophys. Res*, **104** (D10) 12019–12030.

715

716   Perry, L. B., Charles E. Konrad, T. W. Schmidlin, 2007: Antecedent Upstream Air Trajectories

717   Associated with Northwest Flow Snowfall in the Southern Appalachians. *Wea.*

718   *Forecasting*, **22**, 334–352.

719

720   Ralph, F. M., and M. D. Dettinger, 2011: Storms, Floods and the Science of Atmospheric

721   Rivers. *EOS,   Transactions,   Amer.   Geophys.   Union.*, **92**,   265-

722   266, doi:10.1029/2011EO320001.

723

724   Ralph, F. M., P. J. Neiman, and G. A. Wick, 2004: Satellite and CALJET aircraft observations of

725   atmospheric rivers over the eastern North Pacific Ocean during the winter of 1997/98. *Mon.*

726   *Wea. Rev.*, **132,** 1721–1745.

727

      Ralph, F. M., P. J. Neiman, G. A. Wick, S. I. Gutman, M. D. Dettinger, D. R.Cayan, and A.

          B. White, 2006: Flooding   on   California's   Russian   River: Role   of   atmospheric

          rivers. *Geophys. Res. Lett.*, **33,** L13801. doi:10.1029/2006GL026689.

728

729   Rivera, E. R., F. Dominguez, and C. L. Castro, 2014: Atmospheric Rivers and Extreme Cool

730   Season Precipitation Events in the Verde River Basin of Arizona. *J. Hydromet.*, **15**, 813-829,

731   doi: 10.1175/JHM-D-12-0189.1

732

733   Roberge, A., J. R. Gyakum, Eyad H. Atallah, 2009: Analysis of Intense Poleward Water Vapor

734   Transports into High Latitudes of Western North America. *Wea. Forecasting*, **24**, 1732–

735   1747.

736

737   Rutz, J. J., W. J. Steenburgh, and F. M. Ralph, 2014: Climatological characteristics of

738   atmospheric rivers and their inland penetration over the western United States**,**

739   *Mon. Wea. Rev.,* **142**, 905–921. doi: http://dx.doi.org/10.1175/MWR-D-13-00168.1.

740

741   Rutz, J. J., and W. J. Steenburgh, 2012: Quantifying the Role of Atmospheric Rivers in the

742   Interior Western United States, *Atmos. Sci. Let.,* **13**, 257-261.

743

744   Saha, S., and Coauthors, 2010: The NCEP Climate Forecast System Reanalysis. *Bull. Amer.*

745   *Meteor. Soc.*, **91**, 1015–1057.

746

747   Schultz, D. M., and Coauthors, 2002: Understanding Utah Winter Storms: The Intermountain

748   Precipitation   Experiment. *Bull.*   *Amer.*   *Meteor.*   *Soc.*, **83**,   189–210.

749   doi: http://dx.doi.org/10.1175/1520-0477(2002)083<0189:UUWSTI>2.3.CO;2

750

751   Smith, R. A., and C. D. Kummerow, 2013: A Comparison of in Situ, Reanalysis, and Satellite

752   Water Budgets over the Upper Colorado River Basin. *J. Hydrometeor*, **14**, 888–905.

753

754   Steenburgh, W. James, 2003: One Hundred Inches in One Hundred Hours: Evolution of a

755   Wasatch Mountain Winter Storm Cycle. *Wea. Forecasting*, **18**, 1018–1036.

756

757   Steenburgh, W. J., S. F. Halvorson, and D. J. Onton, 2000: Climatology of lake-effect

758   snowstorms of the Great Salt Lake. *Mon. Wea. Rev.*, **128,** 709–727.

759

760   Zhu, Y. and R. E. Newell, 1998: A proposed algorithm for moisture fluxes from atmospheric

761   rivers. *Mon. Wea. Rev.*, **126**, 725-735.

762

763

764

765   Figure Captions

766   Fig. 1 a) Topographic map (m, shading, scale on right) of the western United States and Northern

767   Mexico, that shows the six regions (colored text) used to compute the back trajectories: WA-nID

768   (green), OR-sID (dark blue), NV (orange) UT-CO (light blue), sCA(purple), AZ-NM(yellow),

769   mountain ranges are in black, with the major ranges of the Cascades, Sierra's and Rocky

770   Mountains in larger font; River valleys in *italics*; and station locations are indicated by triangles

771   with the color of their respective region. The black curve, extending along the crest of the

772   Cascade, Sierra and Peninsular Mountains, indicates the position of the cross section shown in

773   Figs. (4-7 and SM8&9). B) Cross section of the topography (in hPa) along the black curve shown

774   in a).

775

776   Fig. 2. a) The 150 maximum one-day precipitation amounts during 1979-2011 at stations within

777   each of the six regions. Only the station with the maximum on a given day is included, although

778   a station could have more than one event among the 150 cases. Open circles show stations

779   without a top event. b) Percentage of the top 150 events occurring at a particular station in each

780   of the regions.

781

782   Fig. 3 Examples of backward trajectories that were initiated near the surface (surface pressure -

783   50 hPa) at the four CFSR grid points around the station at 00Z on the day during which one of

784   150 top precipitation events occurred in the OR-sID region. The dates and precipitation amounts

785   are given above the panels for the four cases. The pressure (hPa) along a trajectory segment is

786   shown by the color (blue-red) scale on the lower right and the terrain height (m) by the (green-

787   white) scale on the bottom left.

788

789   Fig. 4. Count Maps (left) and Cross section (right) indicating the number of back trajectories that

790   pass through a CFSR grid column originating in the a) WA-nID, b) OR-sID, and c) NV regions.

791   The trajectories are initiated at 00, 6, 12 and 18z on days when one of the top 150 (independent)

792   precipitation events occurred. The trajectories are initiated at the four CFSR grid point around

793   the station that recorded the event at a single pressure level located between 50 and 100 hPa

794   above the surface (see text for more details). A total of 2400 trajectories were initiated in each

795   region. The position of a trajectory is estimated at one-hour intervals over the five previous days

796   using the six-hourly three-dimensional CFSR wind fields. Topography is depicted via a 5-point

797   smoother applied to the 30 arc-second (~1 km) terrain height, with contours at 1000 m (3281 ft),

798   1500 m (4921 ft) and 2300 m (7546 ft) and stippling above 2300m. Vertical cross section of the

799   back trajectory counts along the crest of the Cascade, Sierra and Peninsular Mountains (black

800   curve in Fig. 1) for the a) WA-nID, b) OR-sID, and c) NV regions. The terrain is shown in black.

801

802   Fig. 5. As in Fig 4, but for the count maps (left) and cross sections (right) for the top 150 events

803   in the UT-CO, sCA and AZ-NM regions.

804

805   Fig. 6. Count maps (left) and cross sections (right) of the difference between the back trajectories

806   for the top 150 days with precipitation and 300 randomly chosen days (scaled by a factor of 0.5)

807   over the 1979-2011 winters in the WA-nID, OR-sID, and NV regions.

808

809   Fig. 7. As in Fig. 6., but count maps (left) and cross sections (right) of the difference between the

810   top and random back trajectories in the UT-CO, sCA and AZ-NM regions.

811

812

813 Fig. 8. a) The three leading EOFs of the 6-hourly CFSR IVT anomalies, normalized by the local

814 IVT monthly standard deviation, during October-March computed over the western United

815 States. The anomalies are shown as a regression between the principal component (time series)

816 and the normalized anomaly. The percent of variance explained by each EOF is shown in the

817 upper right. b) Histograms of the three leading principal components normalized values.

818

819 Fig. 9. "High" Composites maps constructed from the top 1% (232 6-hourly values) of the first

820 principal component, (PC 1) of the anomalous: IVT (a) magnitude; (b) IVT direction (vectors)

821 and IVT convergence/divergence (shading, convergence = -∇·IVT > 0, mm day^{-1}); (c) 700 hPa

822 specific humidity (q, g kg^{-1}); (d) 500 hPa heigh (dm); (e) precipitation from CFSR (mm day^{-1});

823 and (f) precipitation from Livneh (mm day^{-1}).

824

825 Fig. 10. As in Fig. 9, but for the "High" Composites maps constructed from the top 1% of PC 2

826 values.

827

828 Fig. 11. As in Fig. 9, but for the "Low" Composites maps constructed from the bottom

829 (negative) 1% of PC 2 values.

830

831 Fig. 12. As in Fig. 9, but for the "High" Composites maps based on the top 1% of PC 3 values.

832   To extract a realistic signal from this EOF we also exclude periods that are in the top or bottom

833   1% of PC 2 cases, and retain events where the IVT anomaly is positive in the southwestern US,

834   isolating cutoff lows, leaving 116 events in the composite.

835

836   Fig. 13. Schematic (a) map and (b) cross section along the black line in (a) showing the major

837   moisture pathways from the Pacific Ocean into the intermountain west.

838
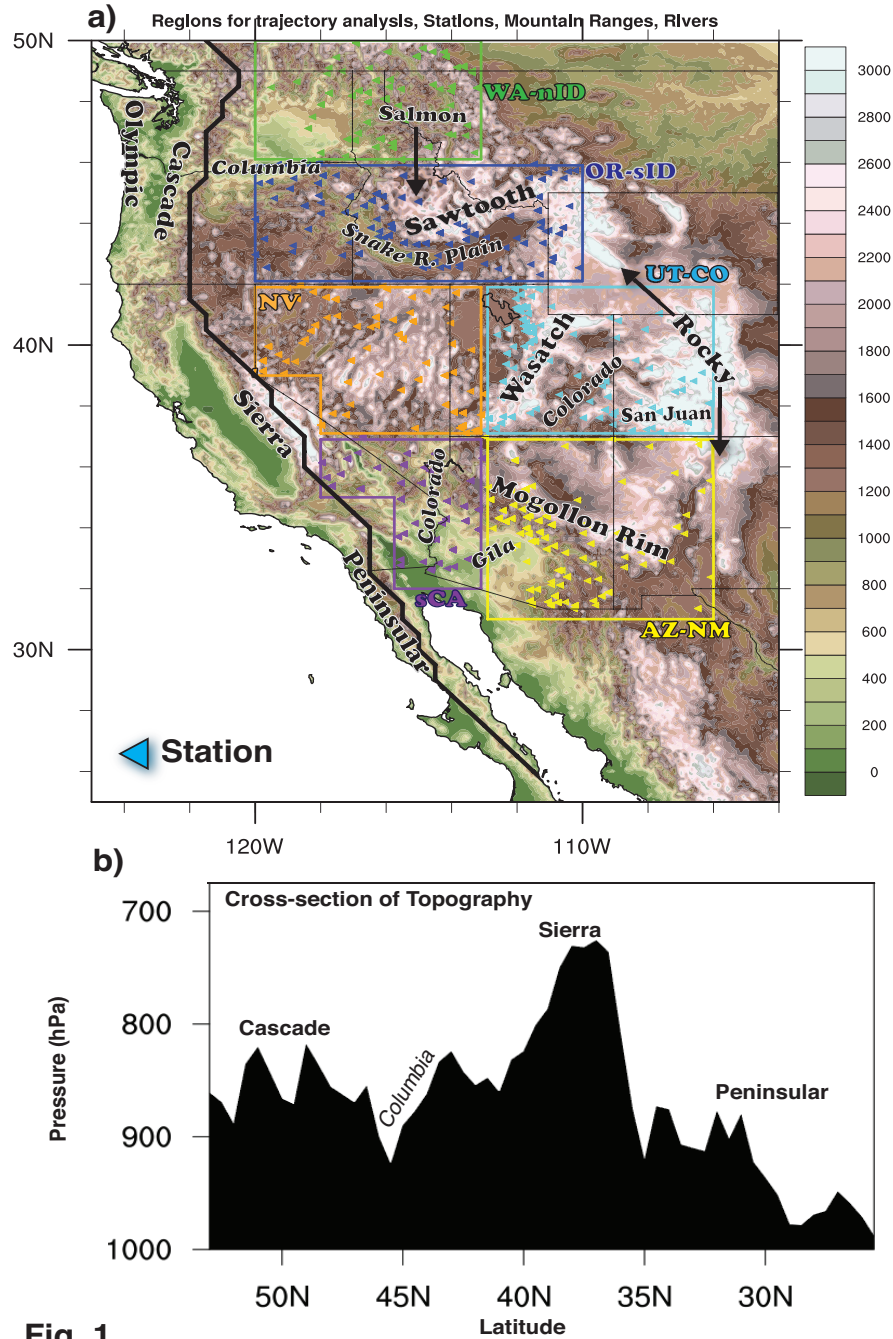
Fig. 1

Fig. 1 a) Topographic map (m, shading, scale on right) of the western United States and Northern Mexico, that shows the six regions (colored text) used to compute the back trajectories: WA-nID (green), OR-sID (dark blue), NV (orange) UT-CO (light blue), sCA(purple), AZ-NM(yellow), mountain ranges are in black, with the major ranges of the Cascades, Sierra's and Rocky Mountains in larger font; River valleys in *italics*; and station locations are indicated by triangles with the color of their respective region. The black curve, extending along the crest of the Cascade, Sierra and Peninsular Mountains, indicates the position of the cross section shown in Figs. (4-7 and SM8&9). B) Cross section of the topography (in hPa) along the black curve shown in a).

848
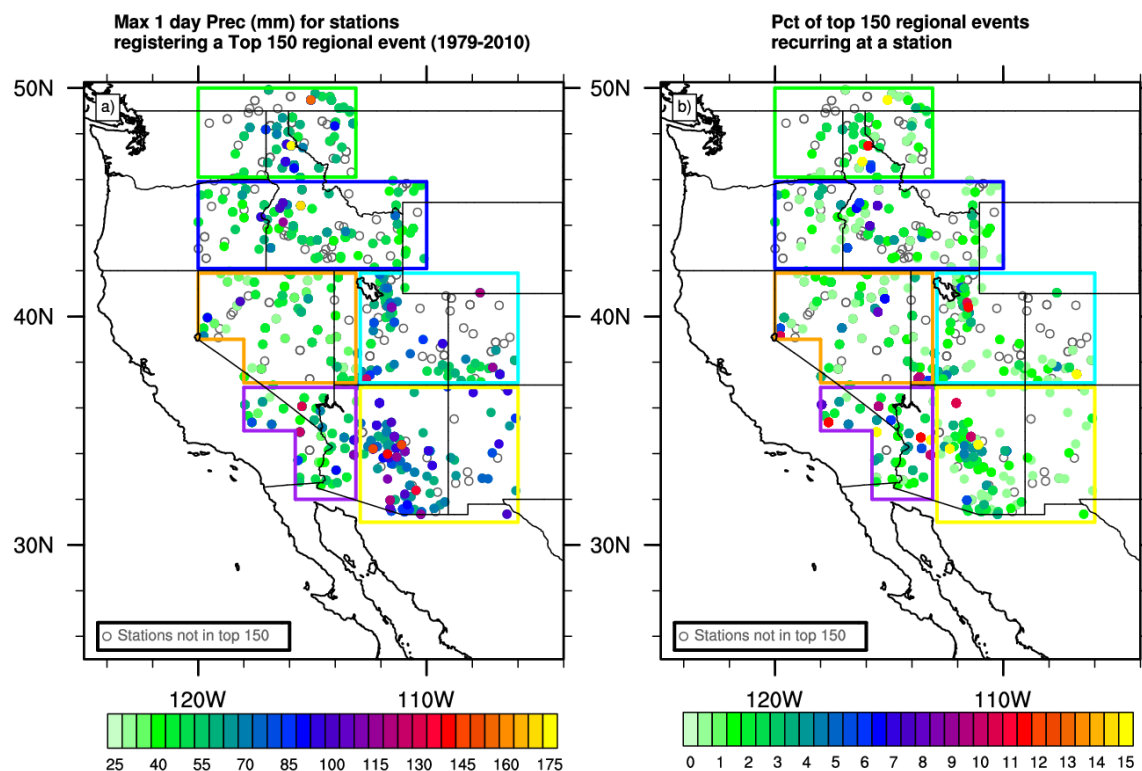
849

850

851

852

Fig. 2. a) The 150 maximum one-day precipitation amounts during 1979-2011 at stations within each of the six regions. Only the station with the maximum on a given day is included, although a station could have more than one event among the 150 cases. Open circles show stations without a top event. b) Percentage of the top 150 events occurring at a particular station in each of the regions.

857
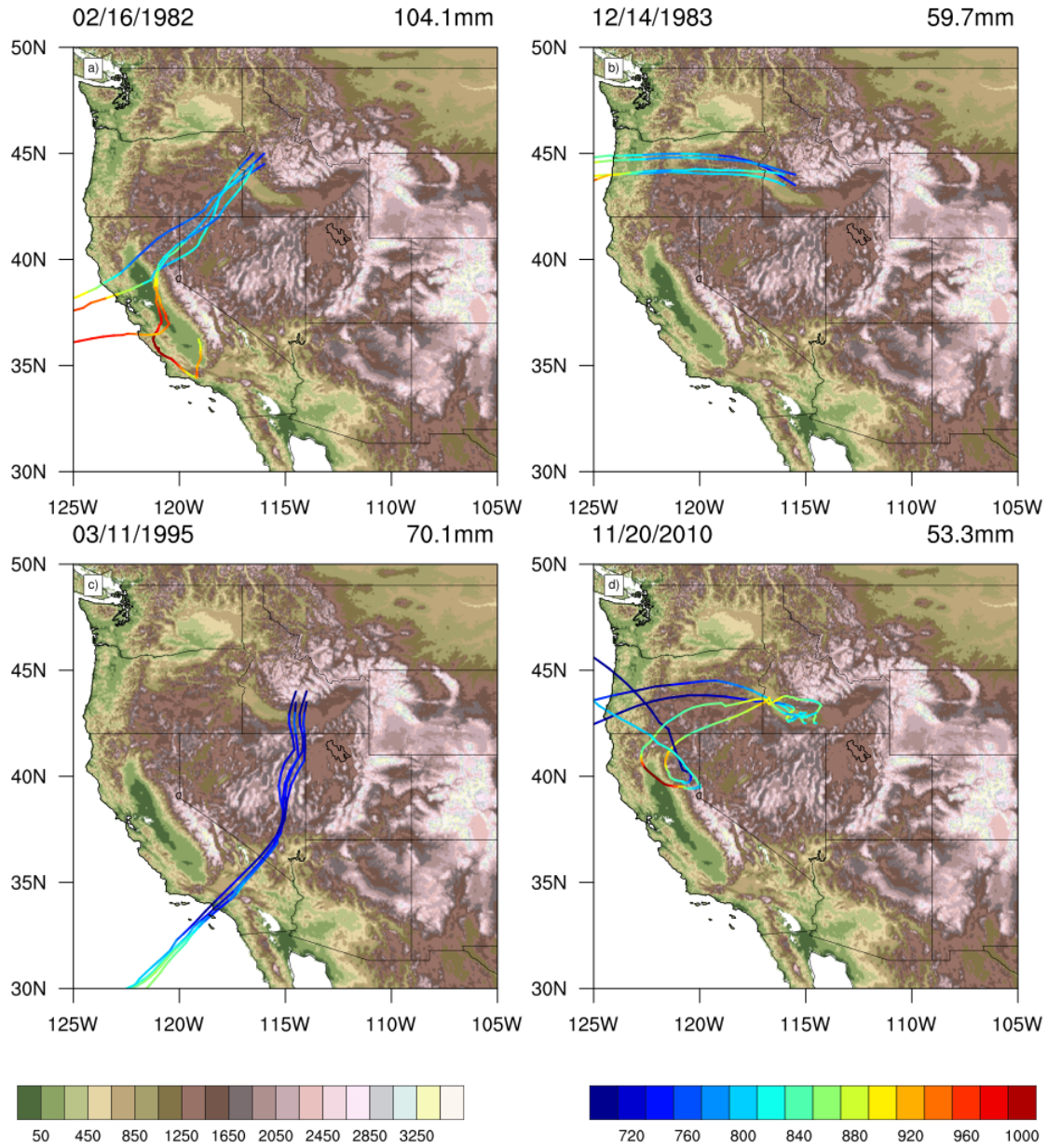
Fig. 3. Examples of backward trajectories that were initiated near the surface (surface pressure - 50 hPa) at the four CFSR grid points around the station at 00Z on the day during which one of 150 top precipitation events occurred in the OR-sID region. The dates and precipitation amounts are given above the panels for the four cases. The pressure (hPa) along a trajectory segment is shown by the color (blue-red) scale on the lower right and the terrain height (m) by the (green-white) scale on the bottom left.
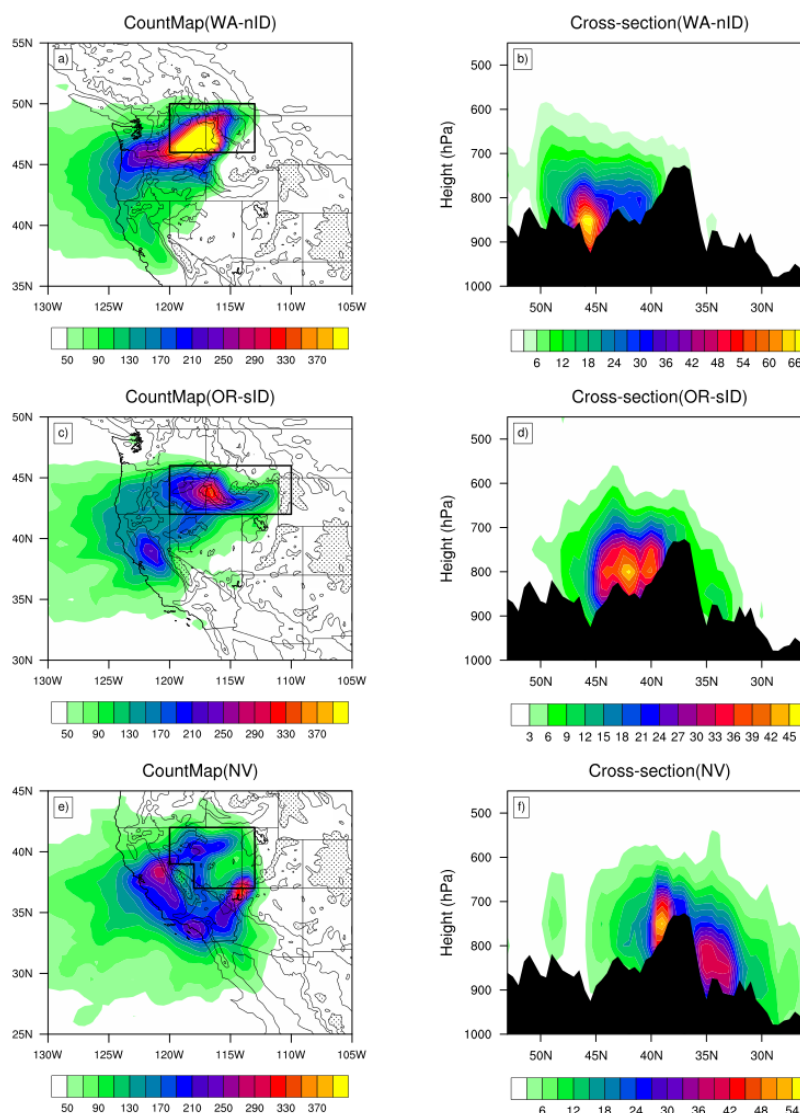
867

868

869

Fig. 4. Count Maps (left) and Cross section (right) indicating the number of back trajectories that pass through a CFSR grid column originating in the a) WA-nID, b) OR-sID, and c) NV regions. The trajectories are initiated at 00, 6, 12 and 18z on days when one of the top 150 (independent) precipitation events occurred. The trajectories are initiated at the four CFSR grid point around the station that recorded the event at a single pressure level located between 50 and 100 hPa above the surface (see text for more details). A total of 2400 trajectories were initiated in each region. The position of a trajectory is estimated at one-hour intervals over the five previous days using the six-hourly three-dimensional CFSR wind fields. Topography is depicted via a 5-point smoother applied to the 30 arc-second (~1 km) terrain height, with contours at 1000 m (3281 ft), 1500 m (4921 ft) and 2300 m (7546 ft) and stippling above 2300m. Vertical cross section of the back trajectory counts along the crest of the Cascade, Sierra and Peninsular Mountains (black curve in Fig. 1) for the a) WA-nID, b) OR-sID, and c) NV regions. The terrain is shown in black.

882

883

884   Fig. 5. As in Fig 4, but for the count maps (left) and cross sections (right) for the top 150 events in the
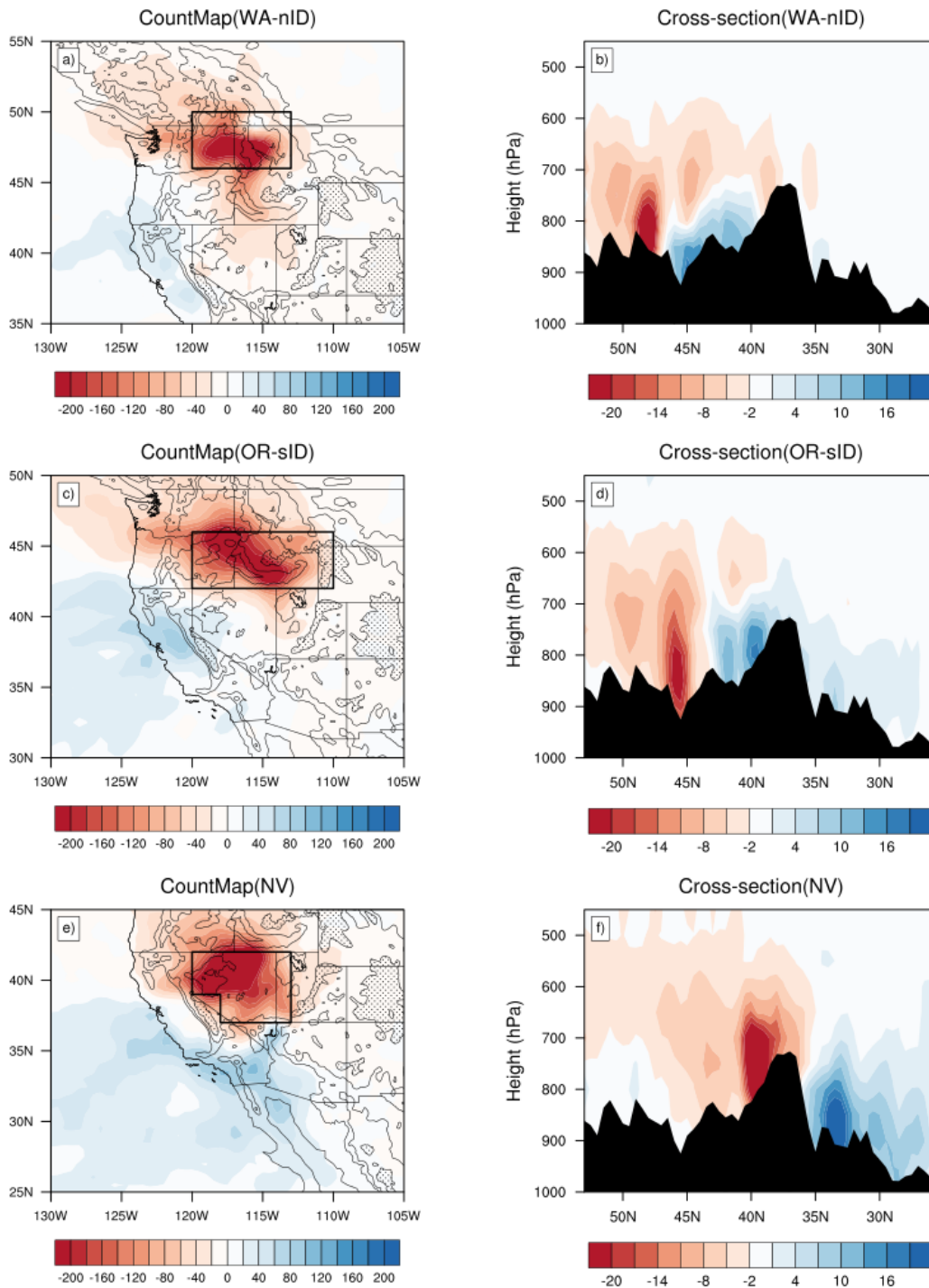885   UT-CO, sCA and AZ-NM regions.

886

887

888　Fig. 6. Count maps (left) and cross sections (right) of the difference between the back trajectories for the
889　top 150 days with precipitation and 300 randomly chosen days (scaled by a factor of 0.5) over the 1979-
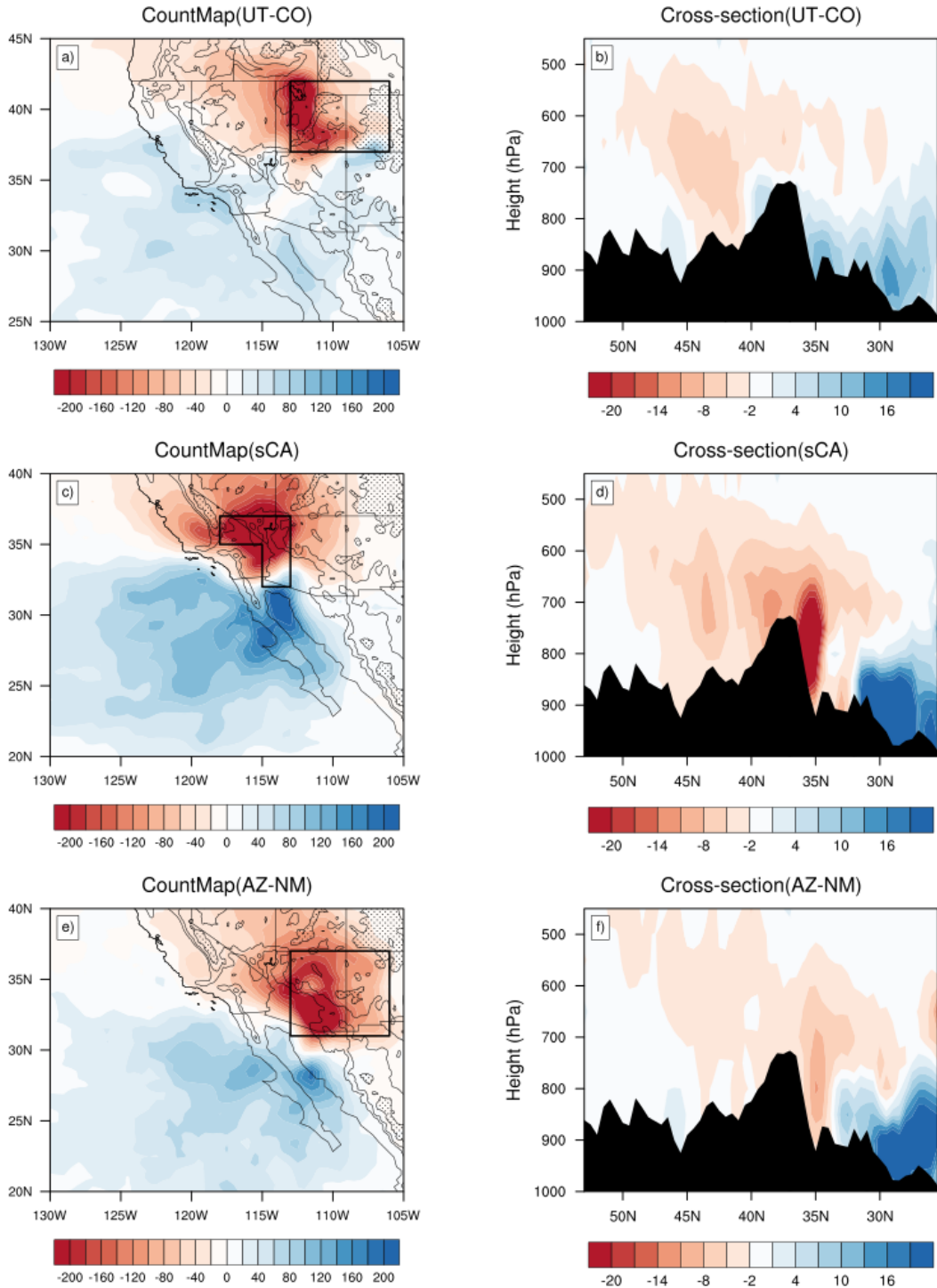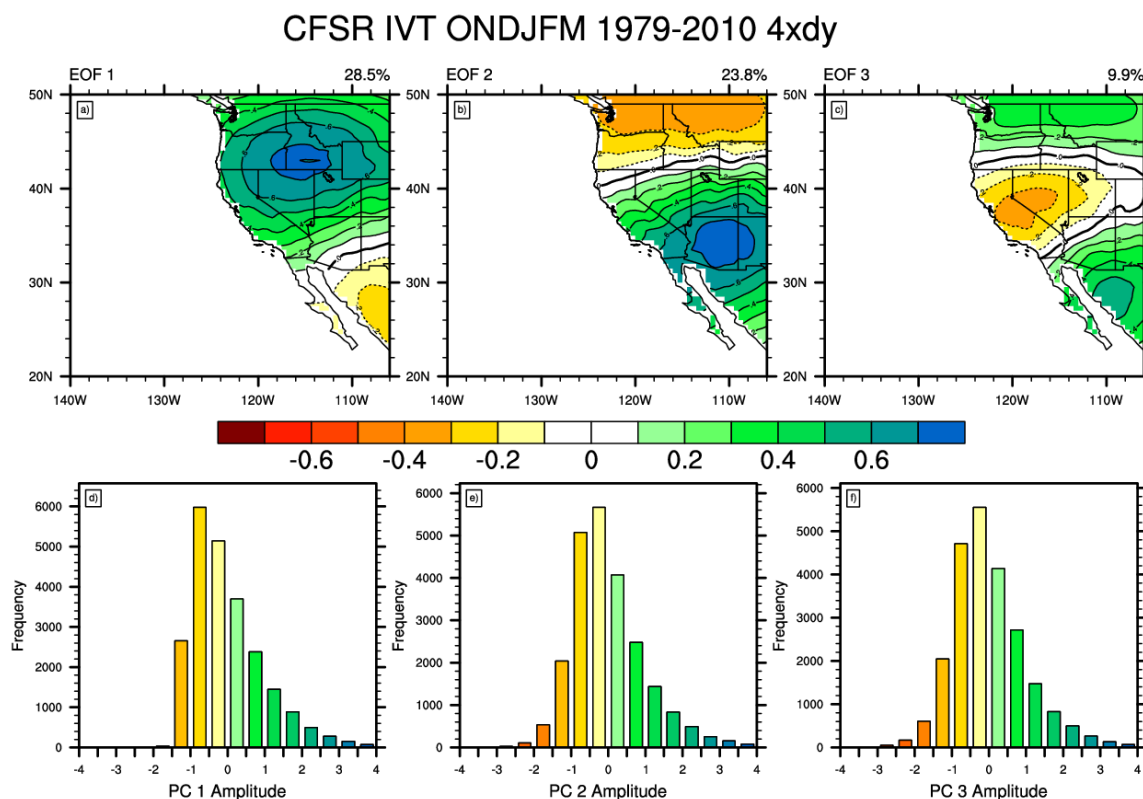890　2011 winters in the WA-nID, OR-sID, and NV regions.

891

894   Fig. 7. As in Fig. 6., but count maps (left) and cross sections (right) of the difference between the top and
895   random back trajectories in the UT-CO, sCA and AZ-NM regions.

896

897

CFSR IVT ONDJFM 1979-2010 4xdy

898
899
900
901

Fig. 8. a) The three leading EOFs of the 6-hourly CFSR IVT anomalies, normalized by the local IVT monthly standard deviation, during October-March computed over the western United States. The anomalies are shown as a regression between the principal component (time series) and the normalized anomaly. The percent of variance explained by each EOF is shown in the upper right. b) Histograms of the three leading principal components normalized values.

907

CFSR IVT ONDJFM EOF 1 high 1.0% Anom Comp

908

909
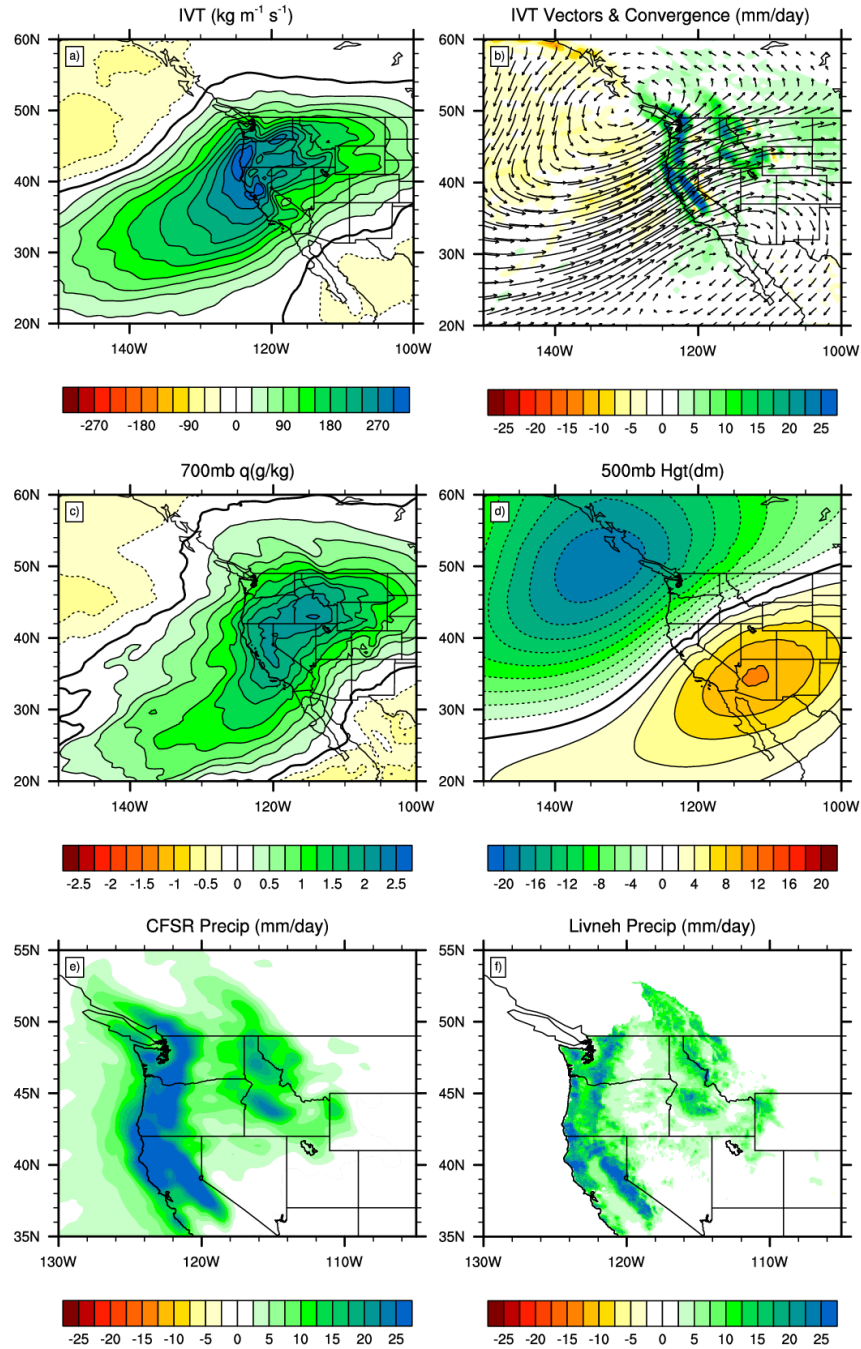
Fig. 9. "High" Composites maps constructed from the top 1% (232 6-hourly values) of the first principal component, (PC 1) of the anomalous: IVT (a) magnitude; (b) IVT direction (vectors) and IVT convergence/divergence (shading, convergence = -∇·IVT > 0, mm day^{-1}); (c) 700 hPa specific humidity (q, g kg^{-1}); (d) 500 hPa heigh (dm); (e) precipitation from CFSR (mm day^{-1}); and (f) precipitation from Livneh (mm day^{-1}).

CFSR IVT ONDJFM EOF 2 high 1.0% Anom Comp

915

916
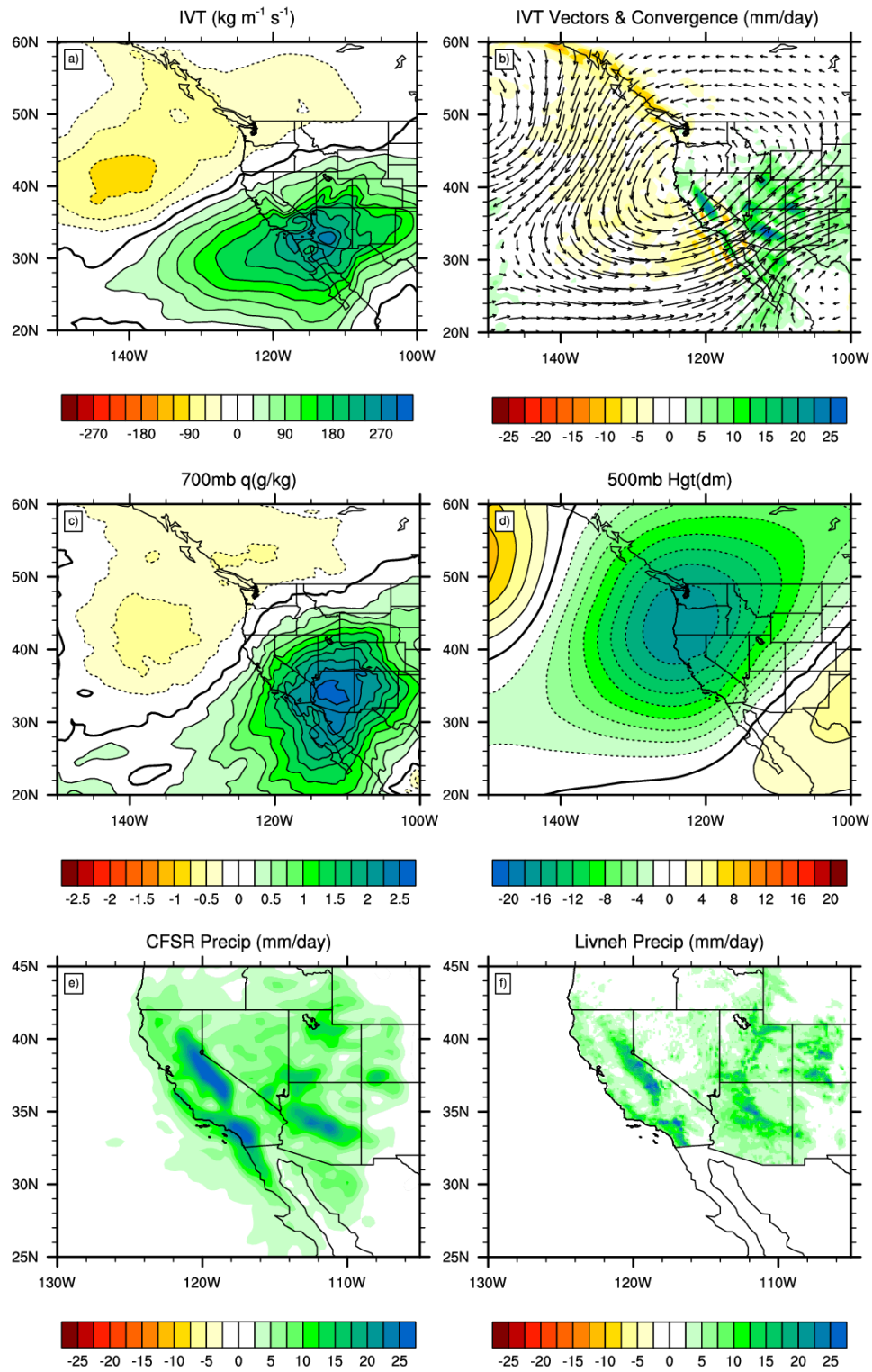
917   Fig. 10. As in Fig. 9, but for the "High" Composites maps constructed from the top 1% of PC 2 values.
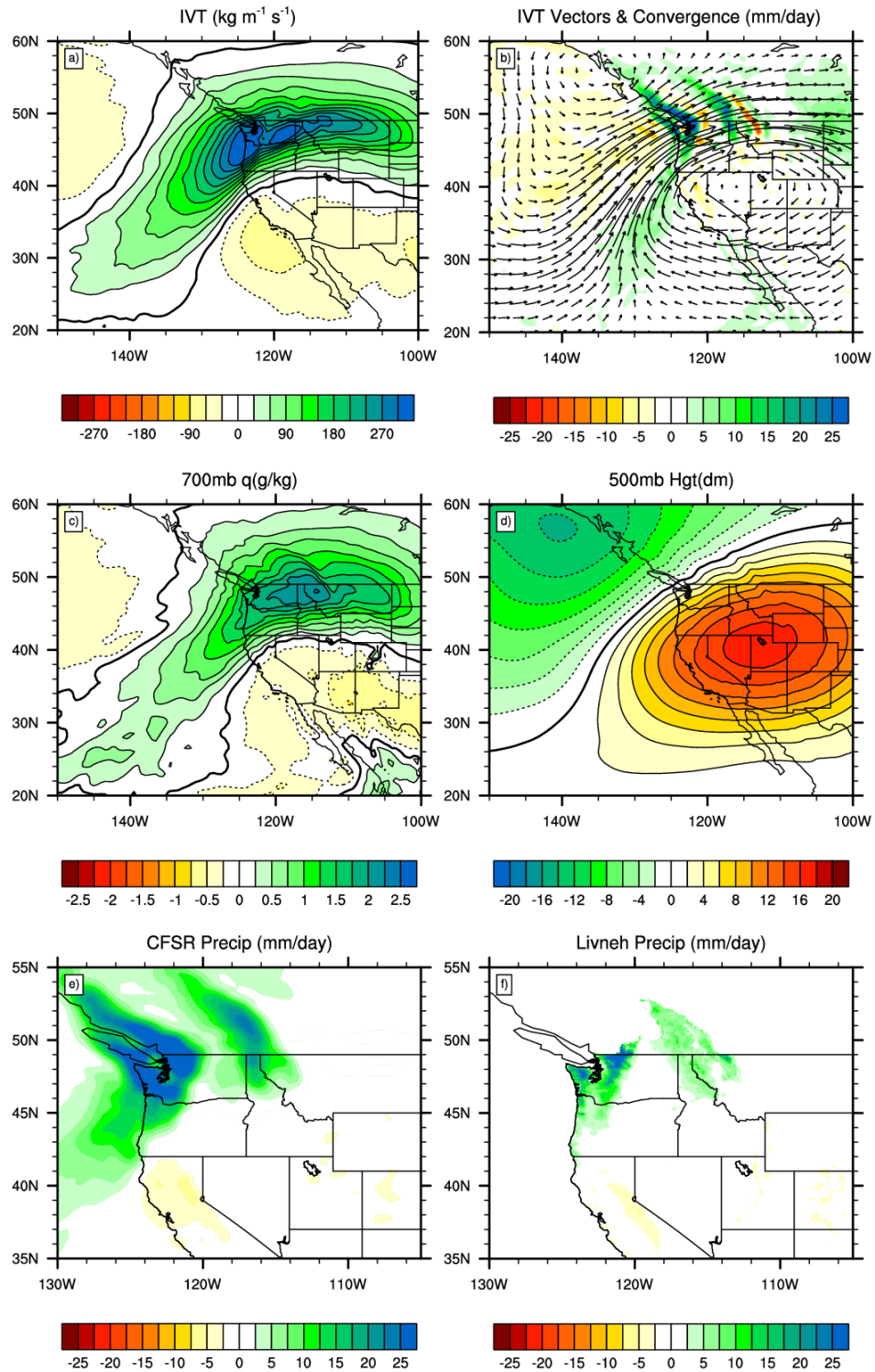
CFSR IVT ONDJFM EOF 2 Low 1.0% Anom Comp

918

919

920   Fig. 11. As in Fig. 9, but for the "Low" Composites maps constructed from the bottom (negative)
921   1% of PC 2 values.

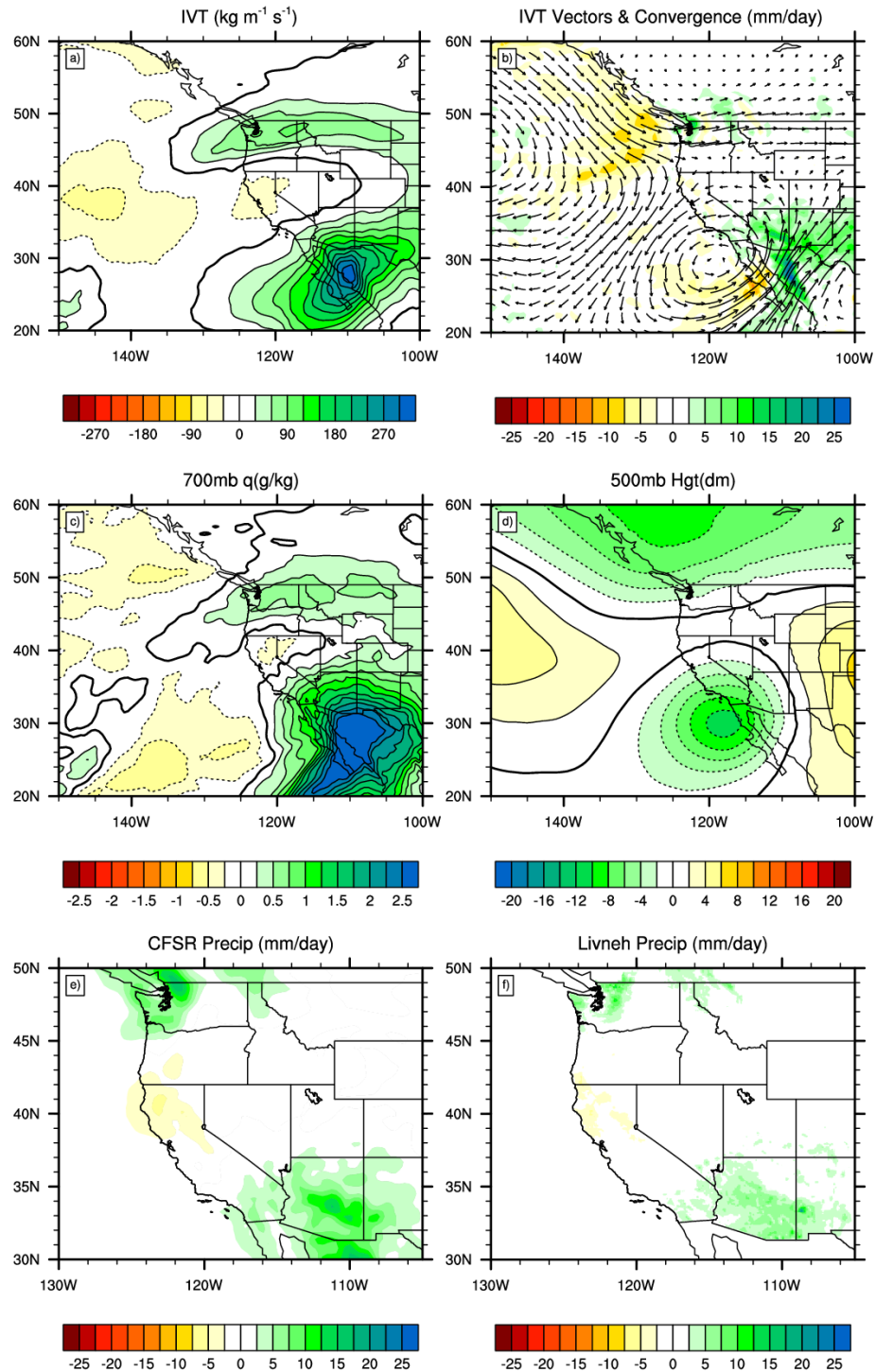## CFSR IVT ONDJFM EOF 3 (modified) high 1.0% Anom Comp
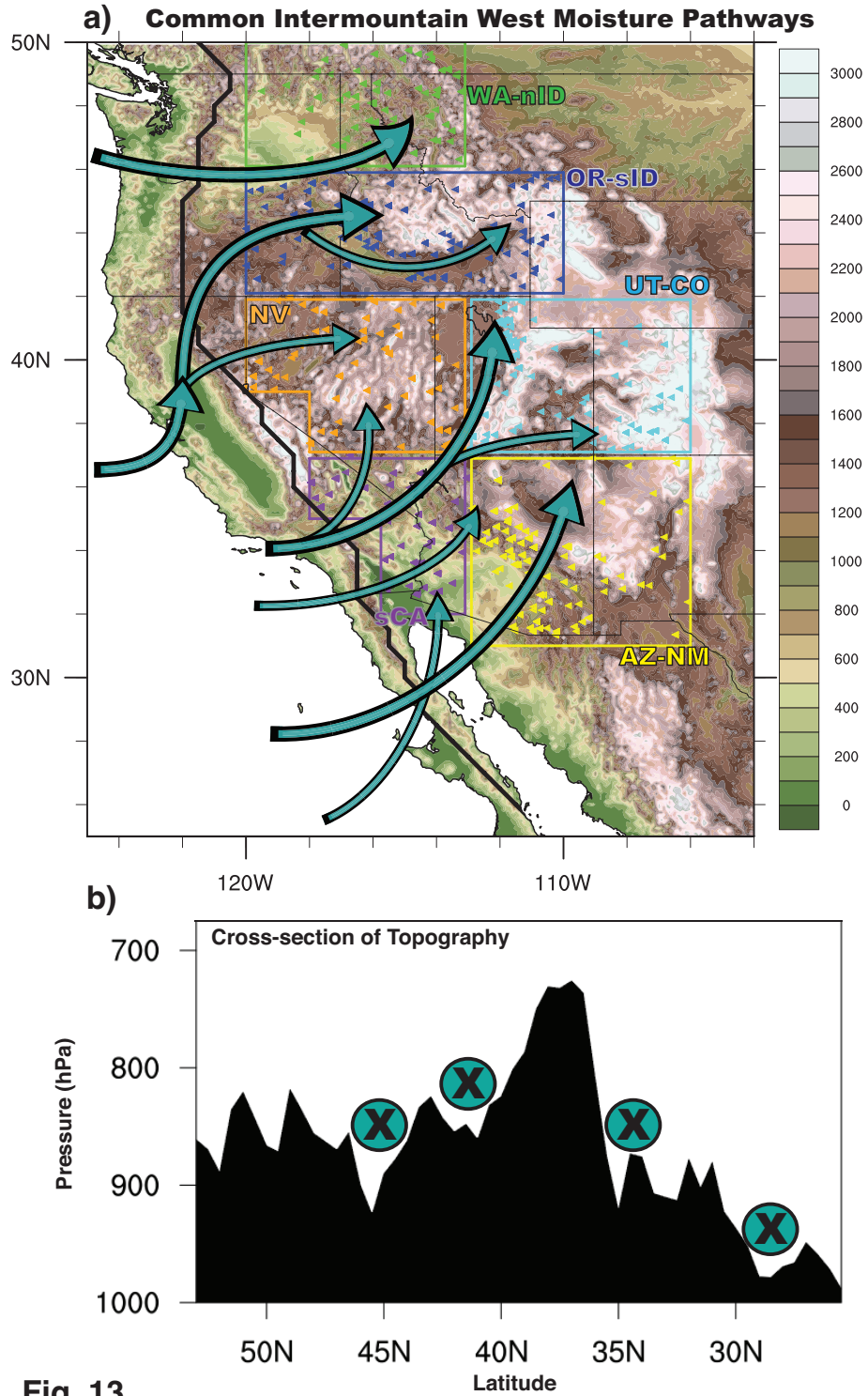

922

923

924   Fig. 12. As in Fig. 9, but for the "High" Composites maps based on the top 1% of PC 3 values. To extract
925   a realistic signal from this EOF we also exclude periods that are in the top or bottom 1% of PC 2 cases,
926   and retain events where the IVT anomaly is positive in the southwestern US, isolating cutoff lows,
927   leaving 116 events in the composite.

Fig. 13

928

929

930   Fig. 13. Schematic (a) map and (b) cross section along the black line in (a) showing the major
931   moisture pathways from the Pacific Ocean into the intermountain west.

932